A Survey of Genuinely Multidimensional Upwinding Techniques[1]

M.E.Hubbard

Numerical Analysis Report 7/93

Department of Mathematics
P.O.Box 220
University of Reading
Whiteknights
Reading
RG6 2AX
United Kingdom

Abstract

Upwind methods have long been popular in the modelling of highly discontinuous flows in one dimension. They have also been frequently used to solve the Euler equations in higher dimensions. However, such attempts have been less successful, since techniques have been used which remain essentially one dimensional and are inadequate for capturing flow features such as shocks or shears not aligned with the grid.

The last ten years have seen a number of attempts to rectify this by introducing genuinely multidimensional physics into the methods. This report gives an overview of one of the most promising groups of methods which has resulted from this quest, and describes in some detail a few of the more important underlying concepts.

Three building blocks are required for these methods: a wave decomposition model, a way to achieve conservation, and a compact advection scheme. Descriptions are given of the contributions of a number of authors to each of these subjects and results are presented which highlight the fact that, despite some success, these methods are still in their infancy.

Contents

1 Introduction

In the past few years upwind methods have become very popular in the modelling of advection dominated flows and in particular those which contain strong discontinuities. For more than a decade, these techniques have been used successfully to solve numerically the one-dimensional Euler equations.

Unfortunately, the extension to higher dimensions is, as always, fraught with problems and has achieved only limited success until recently. Initial attempts were all based on the available one-dimensional methods and modelled the flow by solving simple Riemann problems across cell interfaces. This introduced an undesirable reliance on the computational mesh and such techniques were unable to adequately resolve shocks or shears which were not aligned with the grid. It was soon realised that it was necessary to incorporate genuinely multidimensional physics into these algorithms before the success achieved in one dimension could be repeated.

The first step towards such algorithms was taken by Davis [33] who suggested that the shock capturing capabilities of these methods could be improved by rotating the Riemann problem to align with the direction of physically important flow gradients. This work has since been extended by a number of authors such as Levy, Powell and Van Leer [6, 5], Dadone and Grossman [1] and Tamura and Fujii [35]. An alternative method has been developed independently by Rumsey, Van Leer and Roe [4] and Parpia [13], which calculates multidimensional wave decompositions from two input states by minimising wave strengths and uses these to reconstruct the solution at the next time level. Common to all these methods, though, is the fact that the multidimensional physics is added at the cell interfaces, thus retaining some one-dimensional aspects.

The third group of methods to be developed is the closest to genuinely multidimensional upwinding that has yet appeared and these techniques will be discussed in this report. These methods involve two distinct steps for the solution of the multidimensional Euler equations:

1) The construction of suitable schemes for the solution of the multidimensional linear advection equation. This has involved the development of 'fluctuation distribution' techniques in several dimensions. These may be considered as being somewhere between cell vertex finite volume methods and finite element methods. They use a piecewise continuous linear data representation, and involve the calculation of the fluctuation (or residual) within each cell and its distribution in an upwind manner to update the flow variables at the vertices. A detailed description of these schemes may be found in [32, 26] and their extension to three dimensions is given in [11].

2) The identification of the relevant propagation properties and directions within each cell, *ie.* some form of pattern recognition, which depends on the system of equations under consideration. This requires the development of a wave decomposition model which splits the fluctuation into components each of which corresponds to a simple wave solution of the Euler equations. The fluctuation due to each scalar wave can then be distributed using an advection scheme from step 1). Three types of decomposition, each due to a different author, are described in this report. Roe, [24, 25] and later [29], developed a number of wave models based on simple waves, while Rudgyard [18, 19] has recently developed his own simple wave models which, although similar, have different origins. Deconinck, Hirsch and Peuteman [10] devised an alternative strategy for decomposing the fluctuation. It is based on an attempt to diagonalise the system of Euler equations and results in a set of maximally decoupled equations. Further details of these wave models may be found in [8, 19].

No single paper gives a detailed description of all the aspects of multidimensional upwinding, although Van Leer [16] and Roe and Deconinck [27, 9] give a good overview of all the techniques used above. A more thorough description of all the methods can be found by sampling notes from the VKI Lecture Series *eg.* [12, 32, 8, 19]. All of these papers are concerned with the solution of the linear advection equation or, by extension, the Euler equations, but Tomaich and Roe [7] show that the two-dimensional advection/diffusion equation can be solved in a similar way and suggest that a similar route may be used to create solvers for the full compressible Navier-Stokes equations.

The next section of this report covers fluctuation distribution schemes and their derivation. A description is given of a number of linear and nonlinear schemes and a brief comparison is presented highlighting the advantages and disadvantages of each of the most important schemes. Section 3 contains a description of the wave decomposition models due to Roe, Rudgyard and Deconinck/Hirsch and results from the first two of these are presented. Also described is a conservative linearisation of the two-dimensional Euler equations, essential for these methods to be conservative, and a short comment is given on the implementation of the wave models. Section 4 describes one possible avenue for future work in this area: a hybrid approach which only uses the expensive multidimensional methods in regions where they are needed in an attempt to produce a method which is both fast and accurate. The final section highlights a number of points which arise from the results of the previous sections and provides suggestions for future work.

2 Advection Schemes in Two Dimensions

Before attempting to model the full two-dimensional Euler equations it is necessary to consider the numerical solution of the linear advection equation

$$\frac{\partial u}{\partial t} + \vec{a} \cdot \vec{\nabla} u = 0, \tag{2.1}$$

where $\vec{a} \in \Re^2$ is a constant vector. This is to be solved numerically over an arbitrary triangulation of the region Ω, with appropriate conditions being imposed on the boundary of the domain, $\partial\Omega$.
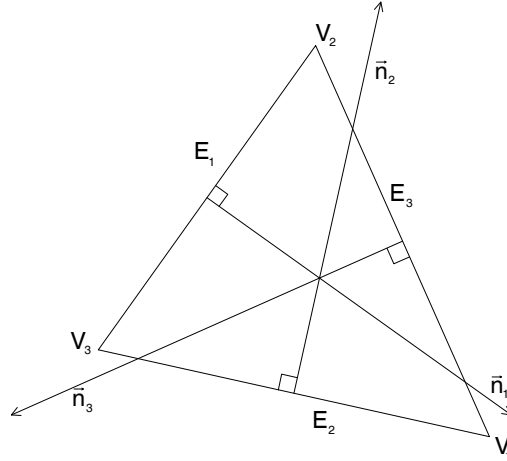

Figure 2.1: A general grid triangle with edges E_i, vertices V_i and normals $\vec{n}_i$.

The solution is represented as piecewise linear over a typical triangle T, such as that in figure 2.1, and can therefore be written as

$$u(x, y, t) = \sum_i u_i(t) w_i(x, y), \tag{2.2}$$

where $w_i(x, y)$ is the 'tent function' used in the application of linear finite elements and $u_i(t)$ can be considered as either the amplitude of w_i or the point value of u at $x = x_i, y = y_i$. Now, the integral of $\frac{\partial u}{\partial t}$ over an element T gives the fluctuation,

$$\phi_T = \iint_{S_T} \frac{\partial u}{\partial t} \, dx \, dy = -\iint_{S_T} \vec{a} \cdot \vec{\nabla} u \, dx \, dy = \oint_{\partial T} u \, \vec{a} \cdot d\vec{n}, \tag{2.3}$$

where ∂T is the boundary and S_T the area of T, and $d\vec{n}$ is the inward normal to the boundary of the element. Note that the fluctuation is related to the cell residual R_T through $\phi_T = -S_T R_T$, where S_T is the cell area, so the two can be easily interchanged in the theory presented below. Now, u varies linearly within each triangle, and hence along each side, so the fluctuation can be easily evaluated:

$$\begin{aligned}
\phi_T &= \frac{1}{2}(u_1 + u_2)\vec{a} \cdot \vec{n}_3 + \frac{1}{2}(u_2 + u_3)\vec{a} \cdot \vec{n}_1 + \frac{1}{2}(u_3 + u_1)\vec{a} \cdot \vec{n}_2 \\
&= -\frac{1}{2}u_1 \, \vec{a} \cdot \vec{n}_1 - \frac{1}{2}u_2 \, \vec{a} \cdot \vec{n}_2 - \frac{1}{2}u_3 \, \vec{a} \cdot \vec{n}_3,
\end{aligned} \tag{2.4}$$

where $\vec{n}_i$ is the *inward* normal to edge i scaled by the length of edge i. Thus, the fluctuation can be expressed simply as

$$\phi_T = -\sum_{i=1}^{3} k_i u_i, \tag{2.5}$$

where

$$k_i = \frac{1}{2} \vec{a} \cdot \vec{n}_i. \tag{2.6}$$

The k_i are important because they can be used to determine the direction of flow through an edge: if $k_i > 0$ then flow enters the triangle through edge i but if $k_i < 0$, edge i is an outflow edge. It is also useful to note that, since

$$\vec{n}_1 + \vec{n}_2 + \vec{n}_3 = \vec{0}, \tag{2.7}$$

we can write

$$\sum_{i=1}^{3} k_i = 0, \tag{2.8}$$

which leads to a number of alternative formulae for ϕ_T which will be used later.

Now, integrating the first term of equation (2.1) over the whole domain using the expression (2.2) gives

$$\int\int \frac{\partial u}{\partial t} \, dx \, dy = \sum_{cells} \frac{1}{3} \left(\frac{\partial u_1}{\partial t} + \frac{\partial u_2}{\partial t} + \frac{\partial u_3}{\partial t} \right) S_T = \sum_{nodes} \frac{\partial u_i}{\partial t} S_i, \tag{2.9}$$

where S_i is the area of the median dual cell around node i, *ie.* one third the total area of the triangles having i as a vertex. By using a simple backward time differencing this leads naturally to a fluctuation distribution scheme where, for each triangle of the domain in turn, three replacements are carried out:

$$S_i u_i \rightarrow S_i u_i + \alpha_i^T \Delta t \, \phi_T. \tag{2.10}$$

The α_i^T are simply weights which determine the distribution of the fluctuation ϕ_T to the nodes of the triangle. It can easily be shown that this gives a conservative scheme provided

$$\sum_{i=1}^{3} \alpha_i^T = 1 \quad \forall T. \tag{2.11}$$

All the schemes that will be considered from now on are restricted so that a given triangle sends only contributions to its own vertices. The resulting schemes then have compact stencils for a given mesh point i, which contain at most the vertices of all triangles with a vertex at node i. After assembling the contributions from all triangles T, meeting at node i, the scheme obtained is

$$u_i^{n+1} = u_i^n + \frac{\Delta t}{S_i} \sum_T \alpha_i^T \phi_T, \tag{2.12}$$

4

which for a given triangle can be written

$$
\begin{aligned}
S_1 u_1^{n+1} &= S_1 u_1^n - \alpha_1^T \Delta t (k_1 u_1^n + k_2 u_2^n + k_3 u_3^n) + TFOT \\
S_2 u_2^{n+1} &= S_2 u_2^n - \alpha_2^T \Delta t (k_1 u_1^n + k_2 u_2^n + k_3 u_3^n) + TFOT \\
S_3 u_3^{n+1} &= S_3 u_3^n - \alpha_3^T \Delta t (k_1 u_1^n + k_2 u_2^n + k_3 u_3^n) + TFOT, \quad (2.13)
\end{aligned}
$$

where TFOT stands for 'terms from other triangles'.

It is the 'fluctuation distribution' form (2.13) that will be considered from now on, and not the nodal form (2.12), since it can be used to treat each cell individually and, with the above restriction, the activity within a cell only affects the nodes at its own vertices.

A basis has now been created for the design of advection schemes on linear triangles, but it is now necessary to decide how the fluctuation within each triangle should be distributed to its vertices. In doing this, it is necessary to take a number of factors into consideration. It has already been shown that conservation is easily guaranteed and that a compact stencil is ensured for the schemes considered. Two further desirable properties are those of positivity and of linearity preservation, defined below.

Positivity means that every value at the new time level, u_i^{n+1}, can be written as a convex combination of old values. So for a linear scheme, written

$$
u_i^{n+1} = \sum_k c_k u_k^n, \quad (2.14)
$$

where the coefficients c_k are independent of the data u_i^n, positivity requires all the c_k to be positive or zero for each node. Consistency is given by

$$
\sum_k c_k = 1. \quad (2.15)
$$

This guarantees a maximum principle for the discrete steady state solution, thus prohibiting the occurrence of new extrema and imposing stability on the explicit scheme [32]. A stronger but more easily verifiable condition is local positivity which requires that the contribution of each triangle separately is positive.

Linearity preservation requires that the scheme preserves the exact steady state solution whenever this is a linear function in space for an arbitrary triangulation of the domain. This is closely related to the idea of second order accuracy of finite difference schemes, although it is an accuracy requirement on the space discretisation only. This property can be verified using the fact that a scheme of the form (2.13) is linearity preserving if and only if, for any triangle T, the coefficients α_i^T are bounded as ϕ_T tends to zero [32].

It should be noted that, when written in the form (2.13), the only possibilities of having a linear scheme are for the coefficients α_i^T to be independent of the

data, in which case the scheme is linearity preserving, or for

$$\alpha_i^T = \frac{\beta_i^T}{\phi_T}, \tag{2.16}$$

where the β_i^T are linear functions of the data summing to ϕ_T. (The superscripts T will be dropped from now on for ease of notation.) This can be used to prove that a linear scheme of the form (2.14) cannot be both positive and linearity preserving [32], a result which is closely related to Godunov's theorem on the incompatibility between second order accuracy and monotonicity preservation for linear schemes in one dimension.
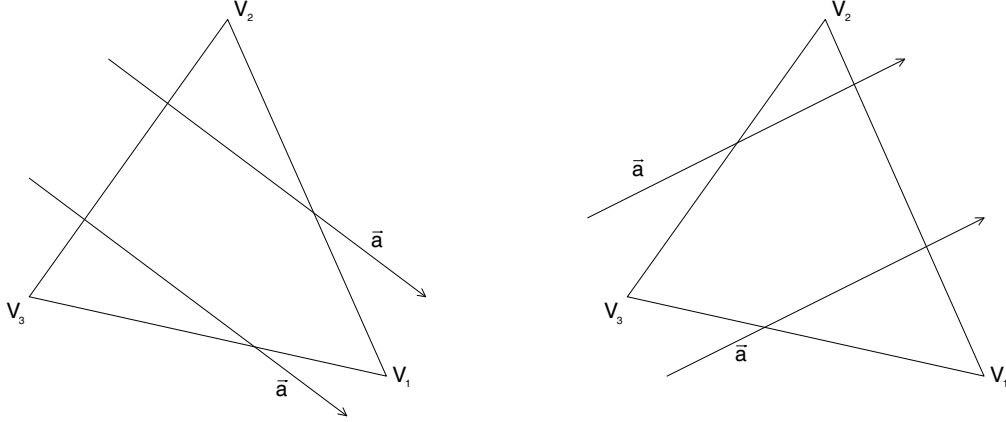

Figure 2.2: A triangle with one inflow side, $k_1 > 0$, $k_2, k_3 < 0$ (left), and one with two inflow sides, $k_1, k_2 > 0$, $k_3 < 0$ (right).

Linear schemes can now be divided into two classes, one satisfying positivity and the other satisfying linearity preservation. If both of these properties are desired then it is necessary to sacrifice the linearity of the scheme. However, at this point, a distinction can be drawn between triangles with one inflow side and those with two inflow sides, figure 2.2. Since each cell can be considered separately, triangles with only one inflow side, say E_1, can have both properties satisfied by sending the whole fluctuation to the downstream node, V_1. This gives a distribution scheme of the form

$$S_1 u_1^{n+1} = S_1 u_1^n - \Delta t (k_1 u_1^n + k_2 u_2^n + k_3 u_3^n) + TFOT, \tag{2.17}$$

with u_2 and u_3 remaining unchanged by the activity within this cell. Therefore it is only the two inflow side case which needs to be considered when developing fluctuation distribution schemes.

2.1 The N Scheme

The first of the schemes to be considered here is called the N scheme. This is a positive linear scheme which is optimal in the sense that it uses the maximum

allowable time step and the most narrow stencil (hence its name, the N(arrow) scheme). A similar optimal scheme has also been derived for use on quadrilateral and hexahedral grids [28].

As explained above, if a triangle within the domain has only one inflow side then the whole fluctuation can be sent to the downstream node, which is the optimal choice. Now, for triangles with two inflow sides, specifying that the scheme is positive means that it cannot be linearity preserving, so the coefficients in equation (2.13) can be expressed as

$$\alpha_i = \frac{\beta_i}{\phi_T}, \tag{2.18}$$

where the β_i are linear functions of the data summing to ϕ_T. Now suppose that the inflow sides are E_1 and E_2, ie. $k_1, k_2 \geq 0$. The upwind philosophy suggests that nothing is sent to the upstream vertex V_3, so

$$\beta_3 = 0 \quad and \quad \beta_1 + \beta_2 = \phi_T. \tag{2.19}$$

Now, making use of (2.8) the fluctuation may be written

$$\phi_T = -k_1(u_1 - u_3) - k_2(u_2 - u_3), \tag{2.20}$$

so the most general two target scheme with linear functions for β_i is,

$$
\begin{aligned}
S_1 u_1^{n+1} &= S_1 u_1^n - \Delta t \left(k_1(u_1^n - u_3^n) + p_1(u_1^n - u_3^n) - p_2(u_2^n - u_3^n) \right) + TFOT \\
S_2 u_2^{n+1} &= S_1 u_1^n - \Delta t \left(k_2(u_2^n - u_3^n) - p_1(u_1^n - u_3^n) + p_2(u_2^n - u_3^n) \right) + TFOT,
\end{aligned}
\tag{2.21}
$$

where p_1 and p_2 are arbitrary parameters, independent of the data and u_3 is unchanged. Now, local positivity of the scheme requires the following quantities to be non-negative:

$$
\begin{aligned}
1 - \frac{\Delta t}{S_1}(k_1 + p_1), \quad p_2, \quad k_1 + p_1 - p_2, \\
1 - \frac{\Delta t}{S_2}(k_2 + p_2), \quad p_1, \quad k_2 + p_2 - p_1.
\end{aligned}
\tag{2.22}
$$

For small enough Δt this is true if

$$p_1, p_2 \geq 0, \quad -k_1 \leq p_1 - p_2 \leq k_2. \tag{2.23}$$

Now, taking non-zero values of p_1 and p_2 can only reduce the allowable time step Δt. Thus, the positive scheme with the maximum allowable time step is

$$
\begin{aligned}
S_1 u_1^{n+1} &= S_1 u_1^n - \Delta t \, k_1(u_1^n - u_3^n) + TFOT \\
S_2 u_2^{n+1} &= S_2 u_2^n - \Delta t \, k_2(u_2^n - u_3^n) + TFOT.
\end{aligned}
\tag{2.24}
$$

7

The restriction placed on the time step by requiring global positivity is obtained by taking into account the coefficients of u_j for all triangles T meeting at node j and gives

$$\Delta t \leq \frac{S_j}{\sum_T \max(0, k_j^T)}. \tag{2.25}$$

This is also the linear scheme with the most narrow stencil, since setting p_1 and p_2 to zero eliminates the contribution from the outermost points of the stencil, figure 2.3a.
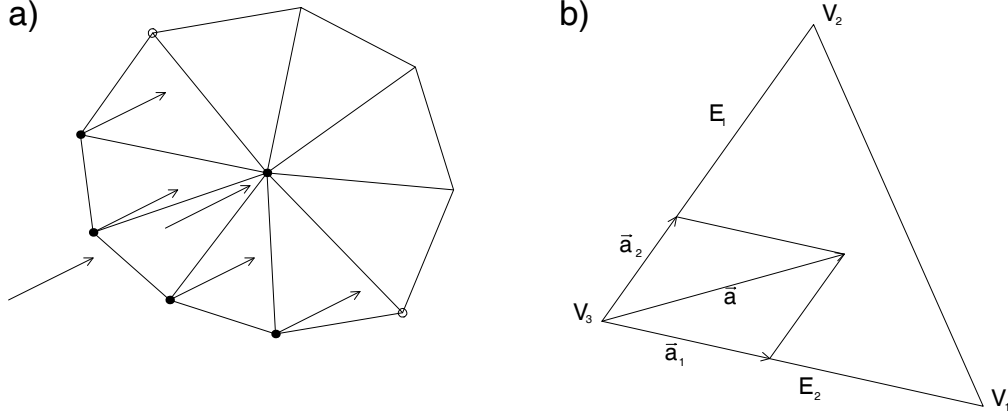

Figure 2.3: The stencil of the N-scheme (left) and the graphical interpretation of the two inflow side case (right).

The effect of this scheme can be easily visualised, figure 2.3b, by considering $\vec{a}$ as the sum of components parallel to E_1 and E_2,

$$\vec{a} = \vec{a}_1 + \vec{a}_2. \tag{2.26}$$

Now, the fluctuation due to $\vec{a}_1$ is sent to V_1 since only E_2 is an inflow side for it, and the fluctuation due to $\vec{a}_2$ is sent to V_2.

2.2 The Low Diffusion Schemes

The next class of linear schemes to be considered are those satisfying linearity preservation. The upwind schemes of this form given here are known as low diffusion schemes due to the relatively small amount of numerical diffusion obtained in comparison with the linear positive upwind schemes.

As before, the single target strategy is used for all triangles with only one inflow side, but for the two inflow side case the general equations (2.13) are considered with the coefficients α_i independent of the data. Two simple strategies can now be found which are both based on dividing the triangle along the velocity vector, as in figure 2.4.
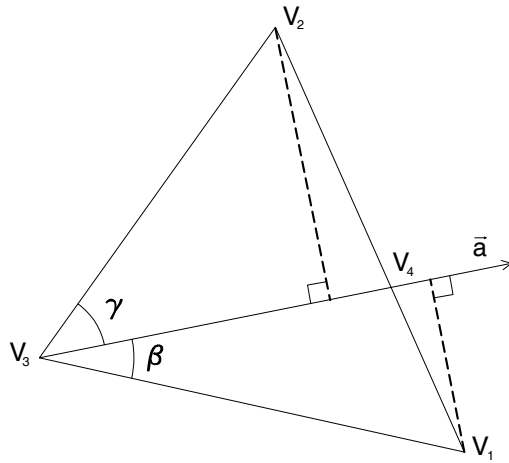
Figure 2.4: The graphical interpretation of the two low diffusion schemes.

The first low diffusion scheme (LDA) is obtained by taking the area of the dividing triangles as the criterion. Referring to figure 2.4, that part of the fluctuation evaluated over sub-triangle 314 is used to update V_2 and the part evaluated over 234 to update V_1. The resulting coefficients α_i are thus given by

$$
\begin{aligned}
\alpha_1 &= -\frac{k_1}{k_3} = \frac{area\ 342}{area\ 123} = \frac{length\ 42}{length\ 12} \\
\alpha_2 &= -\frac{k_2}{k_3} = \frac{area\ 314}{area\ 123} = \frac{length\ 41}{length\ 12}.
\end{aligned}
\tag{2.27}
$$

This then leads to a two target scheme which looks like

$$
\begin{aligned}
S_1 u_1^{n+1} &= S_1 u_1^n - \Delta t \left(\frac{k_1^2}{k_1 + k_2}(u_1^n - u_3^n) + \frac{k_1 k_2}{k_1 + k_2}(u_2^n - u_3^n) \right) \\
S_2 u_2^{n+1} &= S_2 u_2^n - \Delta t \left(\frac{k_1 k_2}{k_1 + k_2}(u_1^n - u_3^n) + \frac{k_1^2}{k_1 + k_2}(u_2^n - u_3^n) \right).
\end{aligned}
\tag{2.28}
$$

An alternative low diffusion scheme (LDB) is obtained using the angles γ and β, figure 2.4, by defining the coefficients α_1 and α_2 as

$$
\alpha_1 = \frac{\sin\gamma\cos\beta}{\sin(\gamma + \beta)}, \qquad \alpha_2 = \frac{\sin\beta\cos\gamma}{\sin(\gamma + \beta)}.
\tag{2.29}
$$

2.3 Other Linear Schemes

There is great emphasis put, in [32], on the fact that many other schemes developed in different ways can be represented using this fluctuation distribution approach. In particular, many finite element techniques are expressed in these terms, although in each case mass lumping is required. It may be that this will provide a structure for analysis for finite volume method such as these by association with finite element schemes. This is also important when considering

a hybrid approach to modelling. Here, different schemes are used in different regions of the flow and it is convenient that all the schemes can be written in a fluctuation distribution form so that the method is consistent throughout the domain.

Two well known central schemes can be easily represented as fluctuation distribution schemes. A Lax-Wendroff type scheme is obtained by defining the coefficients in equation (2.13) to be

$$\alpha_i = \frac{1}{3} + \frac{1}{2}\frac{k_i \Delta t}{S_T}. \tag{2.30}$$

This can be shown to be equivalent to a mass-lumped Taylor-Galerkin finite element method on linear triangles. The choice

$$\alpha_i = \frac{1}{3}, \tag{2.31}$$

obtained by dropping the dissipative contribution in the above scheme is identical with Jameson's [2] central finite volume scheme for unstructured triangular meshes, although it lacks the Runge-Kutta time stepping required to impose stability. It is also equivalent to a mass-lumped Galerkin finite element method on linear triangles. Both of these methods satisfy the linearity preservation property but not positivity.

Alternative upwind schemes may also be represented in this way, including a mass-lumped streamline upwind Petrov-Galerkin (SUPG) finite element method, which gives a linearity preserving scheme, and a first order positive upwind finite volume scheme.

2.4 Nonlinear Schemes

A number of linear schemes have now been described and although all of them are consistent and conservative, none is both positive and linearity preserving. In order to have both these properties, nonlinear schemes must be considered, *ie.* schemes of the form (2.14) where the coefficients depend on the data.

The nonlinear schemes presented here make use of the fact that when considering events within a triangle , the advection velocity $\vec{a}$ can be replaced in the analysis by any vector of the form

$$\vec{a}^* = \vec{a} + \lambda \vec{a}_p, \tag{2.32}$$

where $\vec{a}_p$ is orthogonal to the local value of $\vec{\nabla} u$ and λ is an arbitrary parameter. This is because the addition of this component has no effect on the fluctuation within the cell:

$$(\vec{a} + \lambda \vec{a}_p) \cdot \vec{\nabla} u = \vec{a} \cdot \vec{\nabla} u + \lambda \vec{a}_p \cdot \vec{\nabla} u = \vec{a} \cdot \vec{\nabla} u \tag{2.33}$$
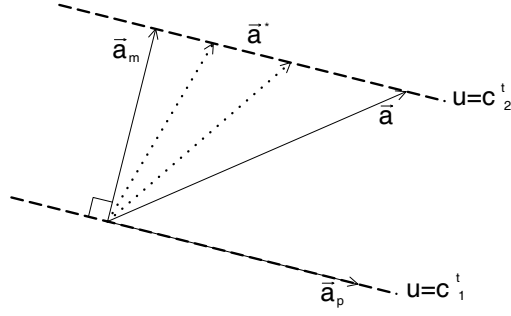
Figure 2.5: The gradient dependent advection velocity.

In particular, the gradient dependent advection velocity, shown in figure 2.5, can be used,

$$\vec{a}_m = (\vec{a} \cdot \vec{m})\vec{m},\tag{2.34}$$

where

$$\vec{m} = \frac{\vec{\nabla} u^n}{|\vec{\nabla} u^n|} = \begin{pmatrix} \cos\theta \\ \sin\theta \end{pmatrix},\tag{2.35}$$

is the unit vector in the direction, θ, of the local gradient of the solution and perpendicular to the level lines of the solution.

Now, since u is assumed to have linear variation in space (so $\vec{\nabla} u$ is constant), the solution of the two-dimensional linear advection problem (2.1) evolves in time according to

$$\begin{aligned} u(\vec{x}, t) &= u_0(\vec{x}_0, t_0) + \vec{\nabla} u \cdot (\Delta \vec{x} - \vec{a}\Delta t) \\ &= u_0(\vec{x}_0, t_0) + |\vec{\nabla} u|(\vec{x} \cdot \vec{m} - |\vec{a}_m|\Delta t) \end{aligned}\tag{2.36}$$

where u_0 represents the initial conditions. These two equivalent forms of the solution to (2.1) show that using the gradient dependent advection velocity still corresponds to the plane wave solution of the linear advection equation, and that using the intrinsically two-dimensional quantity $\vec{a}_m$ corresponds to the notion that waves propagate normal to their level lines.

An important effect of using $\vec{a}_m$ as the advection speed is that, as steady state is approached, $\vec{a}_m$ becomes very small, and so the form of the stability bounds of the N-scheme, (2.25), implies that much larger time steps can be taken as steady state is approached. This is possible because the time scale relevant to stability is that on which a level line of the solution migrates across a cell, not the time taken by a particle moving with velocity $\vec{a}$ [32].

As a consequence of (2.33) any linear combination of $\vec{a}$ and $\vec{a}_m$ can be considered as the advection velocity, and this property is used in the development of appropriate nonlinear schemes.

11

2.5   The NN Schemes

There are two main NN schemes (where NN stands for nonlinear and narrow) which have been developed, both of which use the gradient dependent advection velocity to produce a scheme which is both positive and linearity preserving and, since they are based on the N-scheme described earlier, have a narrow stencil.

The first of these, developed at the VKI, uses the N scheme (2.24), but with the k_i based on the gradient dependent advection velocity, so

$$k_i = \frac{1}{2}\vec{a}_m \cdot \vec{n}_i = \frac{1}{2}(\vec{a} \cdot \vec{m})(\vec{m} \cdot \vec{n}_i),\tag{2.37}$$

where $\vec{m}$ is the unit vector in the direction of $\vec{\nabla}u$ and $\vec{n}_i$ is the scaled inward normal to edge i. Now, since

$$u_1^n - u_3^n = \vec{r}_{31} \cdot \vec{\nabla}u, \qquad u_2^n - u_3^n = \vec{r}_{32} \cdot \vec{\nabla}u\tag{2.38}$$

where $\vec{r}_{ij} = \vec{x}_j - \vec{x}_i$ is the edge vector from vertex i to vertex j of the triangle, then assuming that the inflow sides are E_1 and E_2, figure 2.1, substitution of these values of k_i into equations (2.24) gives

$$
\begin{aligned}
S_1 u_1^{n+1} &= S_1 u_1^n + \Delta t \; \phi_T \frac{(\vec{m} \cdot \vec{n}_1)(\vec{m} \cdot \vec{r}_{31})}{2S_T} + TFOT \\
S_2 u_2^{n+1} &= S_2 u_2^n + \Delta t \; \phi_T \frac{(\vec{m} \cdot \vec{n}_2)(\vec{m} \cdot \vec{r}_{32})}{2S_T} + TFOT,
\end{aligned}\tag{2.39}
$$

where the fluctuation ϕ_T has been introduced, S_T is the area of the triangle under consideration and S_i is the area of the median dual cell around node i. This leads to weights used in the distribution of the fluctuation which are

$$\alpha_1 = \frac{(\vec{m} \cdot \vec{n}_1)(\vec{m} \cdot \vec{r}_{31})}{2S_T}, \qquad \alpha_2 = \frac{(\vec{m} \cdot \vec{n}_2)(\vec{m} \cdot \vec{r}_{32})}{2S_T}.\tag{2.40}$$

These coefficients are now bounded as ϕ_T tends to zero, giving linearity preservation, and positivity has been retained from the N-scheme, so this new method has both the desired properties. Unfortunately, this scheme on its own has been found not to converge in many cases. It has been suggested that this is because when the steady state is approached the gradient of the solution, $\vec{\nabla}u$, tends to be perpendicular to the advection speed, $\vec{a}$, and so the scheme may choose an upstream vertex of a triangle as a target, making the method unstable [32].

This problem is overcome by modifying this method to give a positive, linearity preserving, and far more robust scheme described by the following algorithm:

a) If a triangle has one inflow side according to the plain advection velocity $\vec{a}$ then send all of the fluctuation to the downstream vertex.
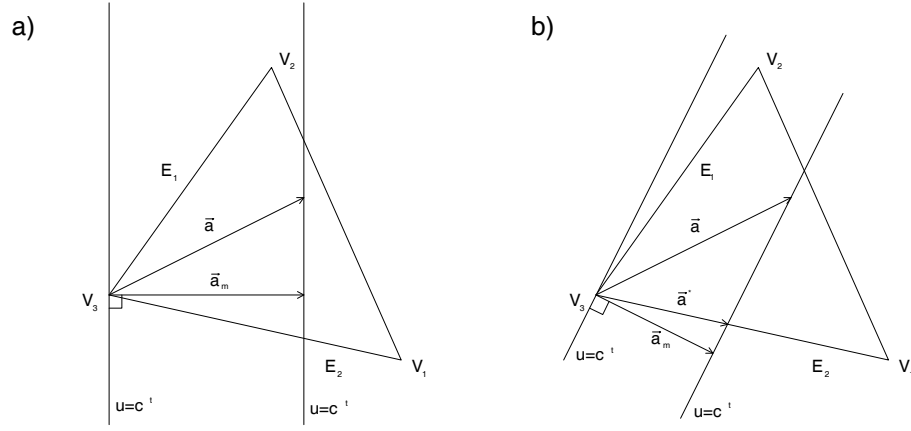
Figure 2.6: The graphical representation of the NN-scheme (VKI).

b) If the triangle has two inflow sides, say E_i and E_j, according to $\vec{a}$, then calculate the gradient dependent advection velocity $\vec{a}_m$.

    i) If $\vec{a}_m$ falls inside the triangle, *ie.* $\vec{a}_m \cdot \vec{n}_i > 0$ and $\vec{a}_m \cdot \vec{n}_j > 0$, then use the two target distribution given by (2.39), see figure 2.6a.

    ii) If $\vec{a}_m$ falls outside the triangle then the distribution (2.39) leads to a non-positive scheme, so use the smallest $\vec{a}^*$ which keeps the scheme positive, figure 2.6b. Hence, if $\vec{a}_m \cdot \vec{n}_i < 0$, $\vec{a}^*$ is chosen parallel with E_j and the whole fluctuation is sent to vertex j. Otherwise the fluctuation is sent to vertex i.

More detailed analysis of this scheme has been carried out by Mesaros and Roe [17], and modifications are suggested to improve the convergence properties still further by ensuring that the distribution coefficients vary continuously as the advection direction rotates from 0 to 2π. This leads to a similar nonlinear narrow scheme which still satisfies positivity and linearity preservation and has been named the PSI scheme.

The second of these nonlinear schemes has been developed by Roe [32]. It has been designed to maximise the allowable time step and is called the level scheme. It is based on the fact that the advection velocity $\vec{a}$ can be replaced in any analysis by a vector of the form (2.32). This leads to

$$k_i = \frac{1}{2}\vec{a}^* \cdot \vec{n}_i = \frac{1}{2}(\vec{a} \cdot \vec{n}_i + \lambda \vec{a}_p \cdot \vec{n}_i) = \frac{1}{2}(\vec{a} \cdot \vec{n}_i + \lambda \vec{\nabla} u \cdot \vec{s}_i), \qquad (2.41)$$

where $\vec{s}_i$ is the vector along E_i (taken anticlockwise around the triangle, figure 2.1). This defines a one parameter family of equally valid alternatives to the

original coefficients k_i^*, given by

$$
\begin{aligned}
k_1 &= k_1^* + \lambda(u_3 - u_2) \\
k_2 &= k_2^* + \lambda(u_1 - u_3) \\
k_3 &= k_3^* + \lambda(u_2 - u_1),
\end{aligned}
\tag{2.42}
$$

which can be chosen to maximise the allowable time step. In [32], it is shown that this is achieved by considering the N scheme (2.24) with the values for the k_i given above and then choosing λ to give the largest possible time step, of the form (2.25). The optimal scheme derived in this way can be interpreted by considering level lines of the solution. If the level line through the downstream vertex passes through the triangle then the optimal time step is obtained by sending the whole fluctuation to one vertex, which depends on the sign of the fluctuation. Otherwise, a two target scheme is used which keeps the direction of $\vec{\nabla} u$ fixed during the update. If the two inflow sides due to the simple advection velocity are E_1 and E_2, then this leads to the coefficients

$$
\alpha_1 = \frac{S_1(u_1 - u_3)}{S_1(u_1 - u_3) + S_2(u_2 - u_3)}, \qquad \alpha_2 = \frac{S_2(u_2 - u_3)}{S_1(u_1 - u_3) + S_2(u_2 - u_3)}, \tag{2.43}
$$

when converted to the form (2.13). This leads to the algorithm:

a) If a triangle has only one inflow side according to the original advection velocity $\vec{a}$, then send the whole fluctuation to the downstream node.

b) If the triangle has two inflow sides, say E_i and E_j, according to $\vec{a}$, then consider the scheme:

     i) If the level line of the solution at the upstream node of the triangle V_k doesn't pass through the triangle, ie. $(u_i - u_k)(u_j - u_k) > 0$, then update both downstream vertices using (2.43).

     ii) If the level line of the solution at V_k does pass through the triangle, send the whole fluctuation to one node, V_i if $(u_i - u_k)\phi_T < 0$, V_j otherwise.

Rudgyard [19] has also devised a positive, linearity preserving scheme which is a variant of Roe's level scheme and has been designed to depend on all aspects of the data in a continuous way in an attempt to improve robustness. The derivation is based on the fact that, if the fluctuation ϕ_T within a cell is negative and u has its minimum value within the cell at node k, then a locally positive scheme will not reduce this value any further. Similarly, for $\phi_T > 0$ the scheme will not increase the maximum nodal value. This leads to a restriction on the time step

ensures that the resulting scheme is positive. Such a method may still update nodes on the upstream side of the cell, affecting convergence, but the distribution coefficients can be chosen to avoid this and to give linearity preservation by remaining bounded as ϕ_T tends to zero:

$$
\begin{aligned}
\alpha_i &= \frac{(k_i^+)^2 (u_i - u_k)}{(k_i^+)^2 (u_i - u_k) + (k_j^+)^2 (u_j - u_k)} \\
\alpha_j &= \frac{(k_j^+)^2 (u_j - u_k)}{(k_i^+)^2 (u_i - u_k) + (k_j^+)^2 (u_j - u_k)} \\
\alpha_k &= 0,
\end{aligned}
\tag{2.44}
$$

where

$$
k_i^+ = \frac{1}{2}(1 + sign(k_i))|k_i|
\tag{2.45}
$$

and node k is chosen so that

$$
\begin{aligned}
u_k &= \min(u_1, u_2, u_3) \quad if \quad \phi_T < 0 \\
u_k &= \max(u_1, u_2, u_3) \quad if \quad \phi_T > 0.
\end{aligned}
\tag{2.46}
$$

The scheme is easily modified to deal with cases when two or more vertices of the triangle have the same value.

As with linear schemes, a number of common nonlinear schemes can be expressed in the form of a fluctuation distribution scheme. In [32], the nonlinear gradient dependent advection velocity has been used to create a scheme of this form equivalent to a mass-lumped SUPG scheme with a shock capturing term.

2.6 Results

In the literature there are two main test cases, introduced by Speckreijse [34], which appear frequently when these schemes are being studied in two dimensions. A small selection of results is presented here simply to highlight some of the most important points.

The first test case consists of linear advection with constant velocity $\vec{a} = (\cos\frac{\pi}{8}, \sin\frac{\pi}{8})$ throughout the unit square $[0, 1] \times [0, 1]$ with boundary conditions $u = 0$ at the lower boundary and $u = 1$ at the left boundary. This problem models a contact or shear discontinuity.

Three different types of grid have been used to produce the results in this report. All of them have been constructed from a cartesian grid. The triangular grids, shown in figure 2.7, have then been produced by inserting diagonals between the bottom left and top right vertices of each square (Grid A), the bottom right and top left vertices (Grid C) and by alternating between the two (Grid B).

Figures 2.8-2.11 show the results of this test case on a grid of type A based on a 33×33 cartesian mesh, using four different schemes, the N scheme, the VKI NN
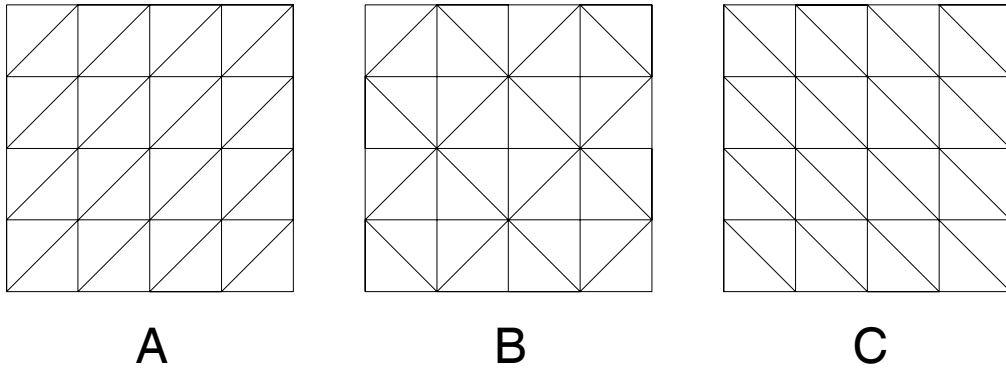
Figure 2.7: The three types of grid used for the results.

scheme, the LDA scheme, and the Lax-Wendroff scheme. The second of these has been chosen as representative of all the nonlinear schemes presented here since they all give very similar results [32]. In each case, the initial conditions used were $u = 1$ on the left boundary, $x = 0$, and $u = 0$ elsewhere and all four schemes gave steady state solutions which converged to machine accuracy.

As expected, the two non-positive schemes, LDA and Lax-Wendroff, give oscillations in the solution close to the discontinuity, with those produced by the Lax-Wendroff scheme being much larger. (The LDB scheme gives much the same results as the LDA scheme.) However, since they satisfy linearity preservation, they also give the sharpest discontinuities, closely followed by the NN scheme which is also linearity preserving. The two positive schemes, N and NN, both give solutions with no oscillations at the discontinuity. The NN scheme gives the sharper definition of the two, although in all cases the shear continues to become more diffuse across the domain. It appears from this that the NN scheme is the best shown here, having both higher order accuracy (experiments have shown it to be roughly of order 1.6) and giving a monotone solution across the discontinuity. As yet, though, it is not clear which of these nonlinear narrow schemes shows the most promise, particularly in its application to the Euler equations.

What this doesn't show is the grid dependence of these algorithms. This is demonstrated in figures 2.12-2.15 which show results from both this case and a second shear test case which differs only in the advection velocity, $\vec{a} = (\cos \frac{\pi}{4}, \sin \frac{\pi}{4})$. Both cases were run on 33×33 grids of types A and C. As can be seen, when the diagonals of the grid are exactly parallel with the advection velocity, the discontinuity is captured extremely well across just one line of cells, but this deteriorates rapidly as the diagonals becomes less aligned with the flow, until the worst case is reached when the diagonals are orthogonal to the flow. In practice grids are unlikely to emulate either of the two extremes, but will produce something closer to the intermediate solutions, figures 2.13 and 2.14. In fact, for a grid of type B, figure 2.9 shows the worst possible grid alignment.

This observation can be considered in two ways. The pessimistic view would be that any grid dependence is undesirable since it leads to much uncertainty over the results, particularly when matters are complicated by considering systems of nonlinear equations. Alternatively, the best result obtained above, figure 2.12, is extremely good, so it may be advantageous to develop a grid adaption algorithm which will align edges of grid cells with the direction of the flow, resulting in very sharp discontinuities. Again, complications will arise when this is extended to the Euler equations, but the potential benefits are huge.

The second of the test cases of Speckreijse consists of clockwise circular advection, with $\vec{a} = (y, -x)$, of a square profile about the point $(0, 0)$ in the rectangular domain $[-1, 1] \times [0, 1]$. The boundary conditions imposed are $u = 0$ at the left boundary and at the lower boundary for $x < -0.65$ and $-0.35 < x < 0$, and $u = 1$ at the lower boundary for $-0.65 < x < -0.35$.

This case was again run to a steady state and all schemes converged to machine accuracy. The initial conditions were $u = 1$ on $y = 0$, $-0.65 < x < -0.35$ and $u = 0$ elsewhere and grids based on a 65×33 cartesian mesh were used. The results in figures 2.16-2.19, produced on a type B grid, really only serve to reiterate the observations made above about the shear test case. Again, and for the same reasons, the NN scheme gives the best results. Grid dependence cannot be seen here but becomes obvious as soon as the non-symmetric grids, A and C, are used. Careful examination then shows that much more cross diffusion is introduced to the solution in the half of the domain where the diagonals are less favourably aligned with the flow. This test case has been used by Roe [15] for experiments to determine the accuracy of the upwind schemes. These show that, practically, the N scheme is somewhat less than first order accurate, the NN schemes are closer to second order accuracy than to first, while the LDA scheme has second order or worse accuracy on general grids but is third order accurate on a regular grid with the diagonals in the 'correct' direction.

It should be pointed out that these results are for steady state problems, as presented in almost all of the literature on the subject. A much more stringent test would be to advect the square profile around the circle for the exact time it should take to reach the outflow boundary. The NN scheme, although still the best, can no longer model this adequately, figure 2.20, and a significant amount of diffusion can be seen at the outflow boundary. Where it fails seriously is on cases where the solution is not being continually augmented by the boundary conditions. If, for example, the circular advection of a 'cone' around the centre of the square domain $[-1, 1] \times [-1, 1]$ is considered, then all of the upwind schemes shown in this section fail to model it with any accuracy. Initially, $u = \cos^2(2\pi r)$ for $r \leq 0.25$ where $r^2 = (x + 0.5)^2 + y^2$, and $u = 0$ elsewhere, figure 2.21. This is then advected with velocity $\vec{a} = (-2\pi y, 2\pi x)$ on a triangulated 65×65 grid of

type B. Even with the NN scheme, after one revolution the peak of the cone has been reduced to only 18.5% of its original value and it has been heavily diffused, figure 2.22. Fortunately, this is not a problem for steady state calculations but improvements to the time accuracy of these schemes will need to be made to these schemes before time varying flows can be modelled with any confidence using these methods.
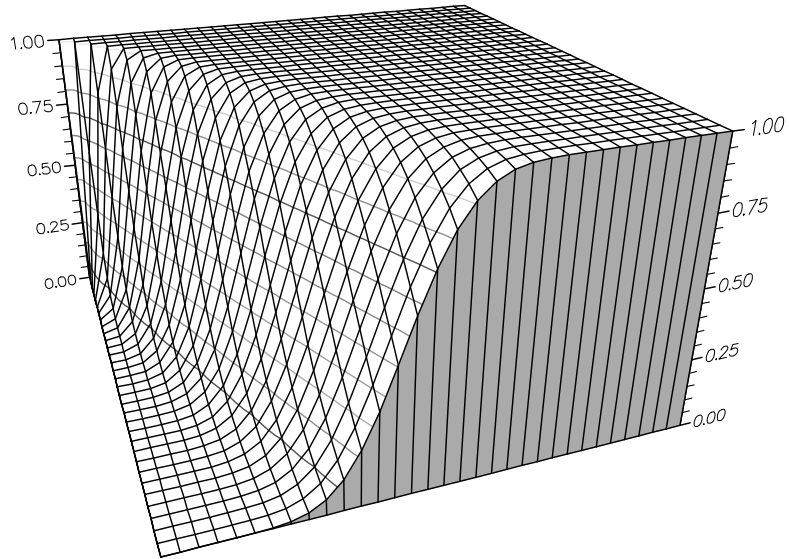
Figure 2.8: Shear test case 1: $\vec{a} = (\cos\frac{\pi}{8}, \sin\frac{\pi}{8})$, N scheme, grid B.
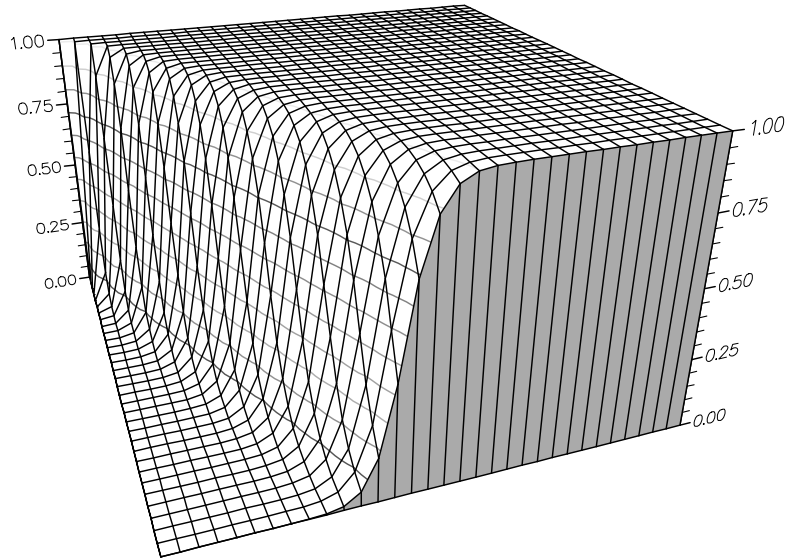
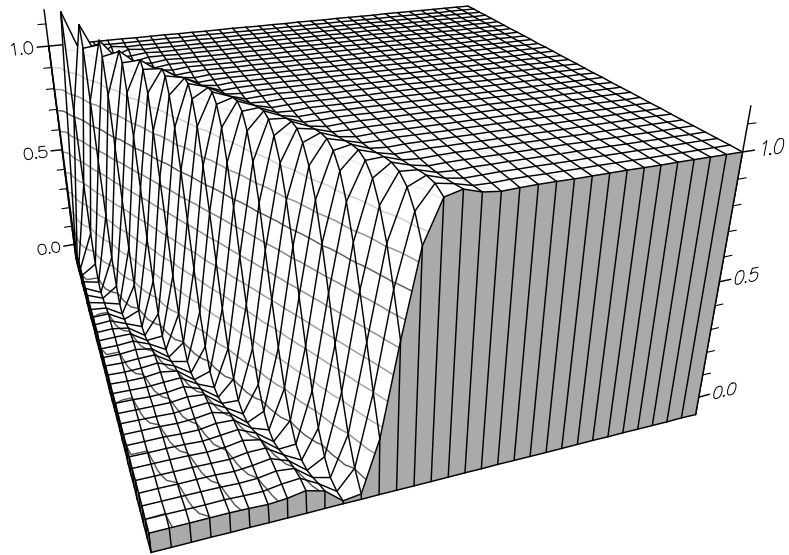Figure 2.9: Shear test case 1: $\vec{a} = (\cos\frac{\pi}{8}, \sin\frac{\pi}{8})$, VKI NN scheme, grid B.

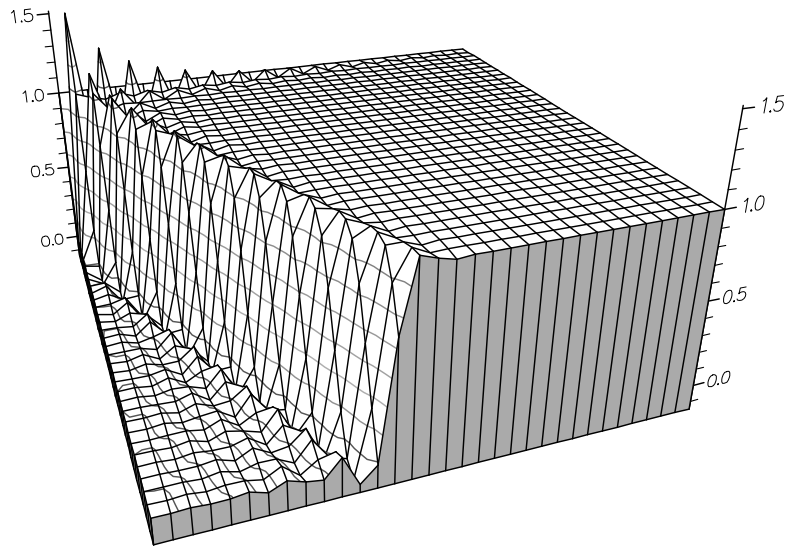Figure 2.10: Shear test case 1: $\vec{a} = (\cos\frac{\pi}{8}, \sin\frac{\pi}{8})$, LDA scheme, grid B.

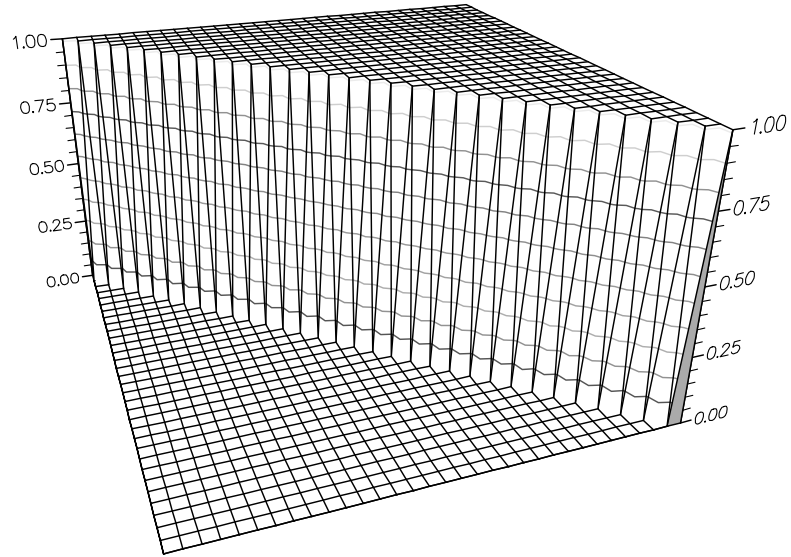Figure 2.11: Shear test case 1: $\vec{a} = (\cos\frac{\pi}{8}, \sin\frac{\pi}{8})$, Lax-Wendroff scheme, grid B.

Figure 2.12: Shear test case 2: $\vec{a} = \left(\cos\frac{\pi}{4}, \sin\frac{\pi}{4}\right)$, VKI NN scheme, grid A.

Figure 2.13: Shear test case 1: $\vec{a} = \left(\cos\frac{\pi}{8}, \sin\frac{\pi}{8}\right)$, VKI NN scheme, grid A.
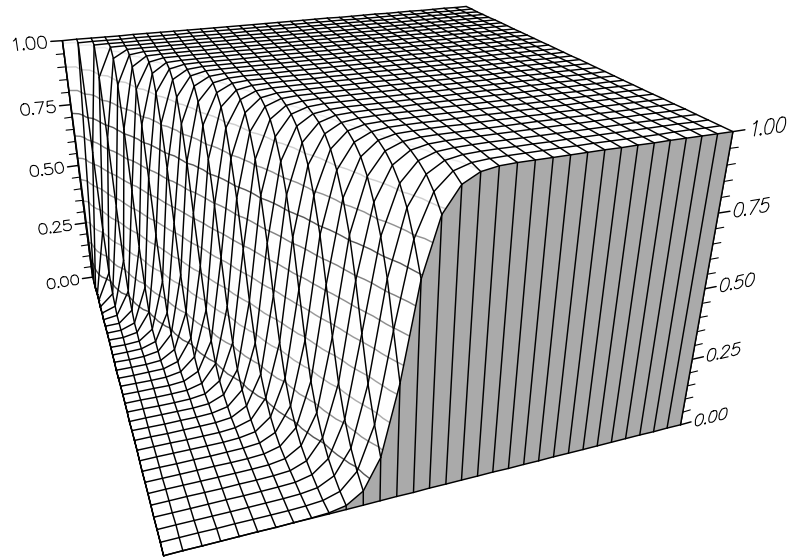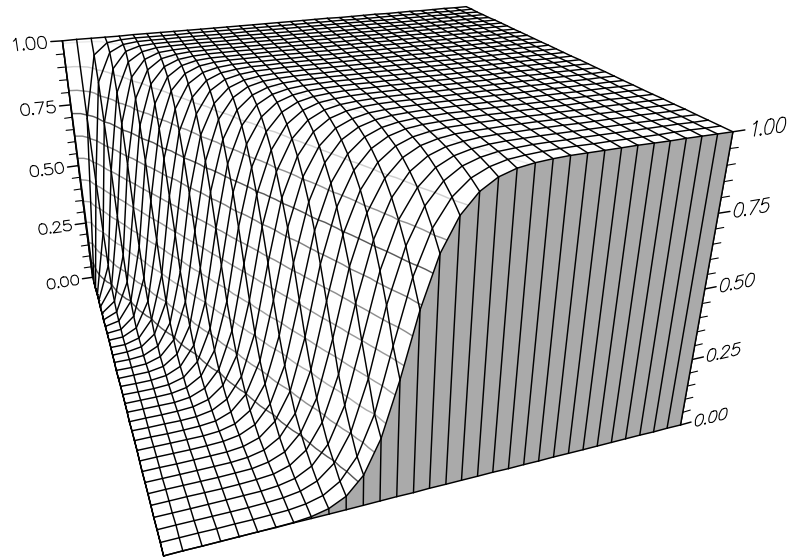
Figure 2.14: Shear test case 1: $\vec{a} = (\cos \frac{\pi}{8}, \sin \frac{\pi}{8})$, VKI NN scheme, grid C.
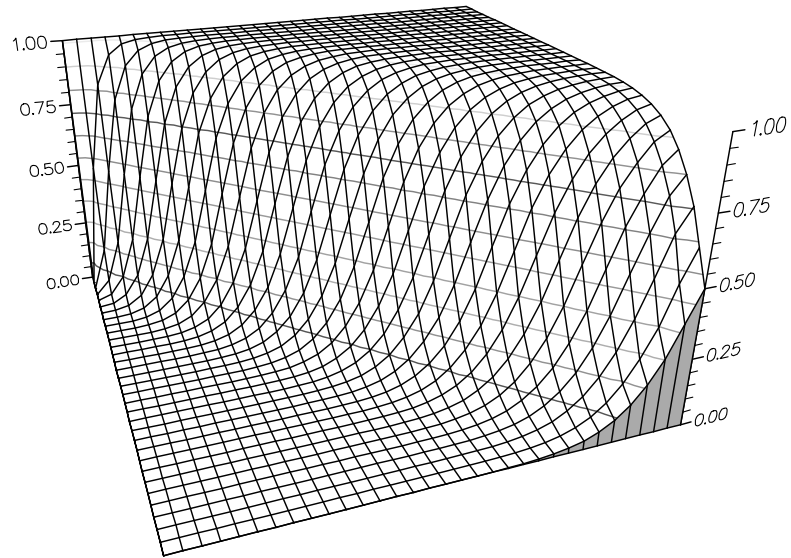

Figure 2.15: Shear test case 2: $\vec{a} = (\cos \frac{\pi}{4}, \sin \frac{\pi}{4})$, VKI NN scheme, grid C.

Figure 2.16: Circular advection test case: $\vec{a} = (y, -x)$, N scheme, grid B.

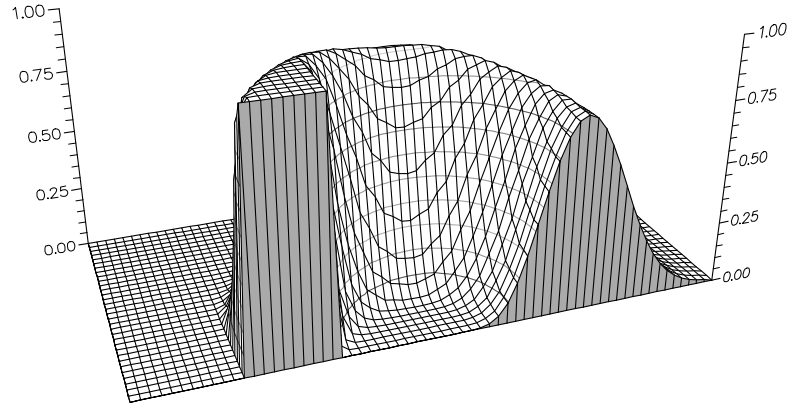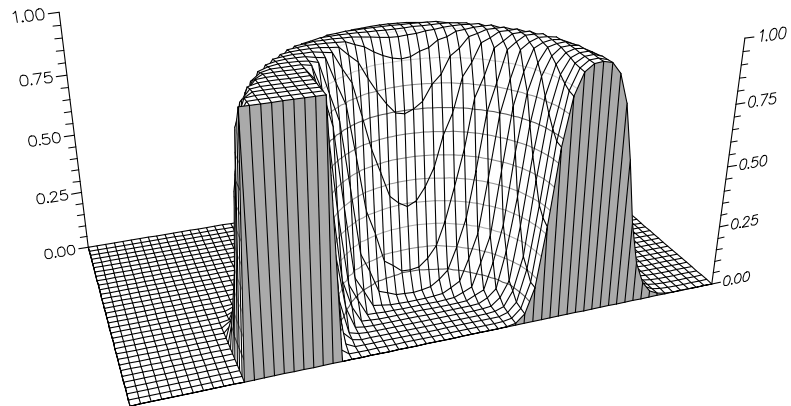Figure 2.17: Circular advection test case: $\vec{a} = (y, -x)$, VKI NN scheme, grid B.

Figure 2.18: Circular advection test case: $\vec{a} = (y, -x)$, LDA scheme, grid B.
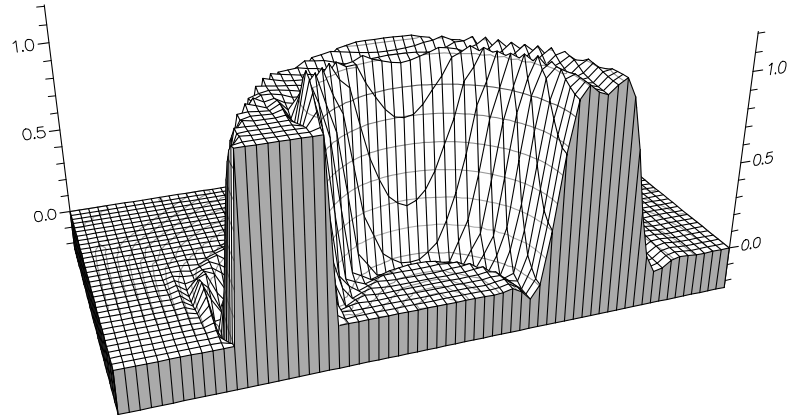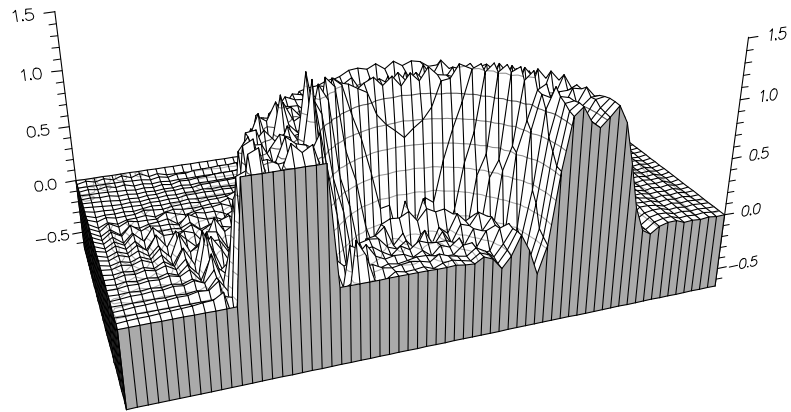

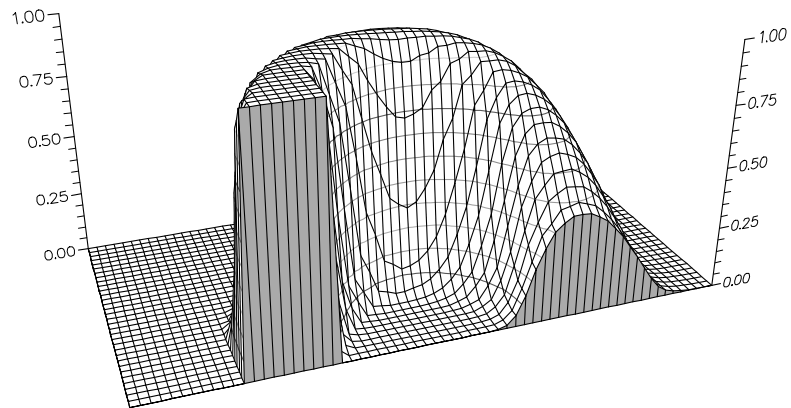Figure 2.19: Circular advection test case: $\vec{a} = (y, -x)$, Lax-Wendroff scheme, grid B.

Figure 2.20: Circular advection test case with $t = \pi$: $\vec{a} = (y, -x)$, VKI NN scheme, grid B.
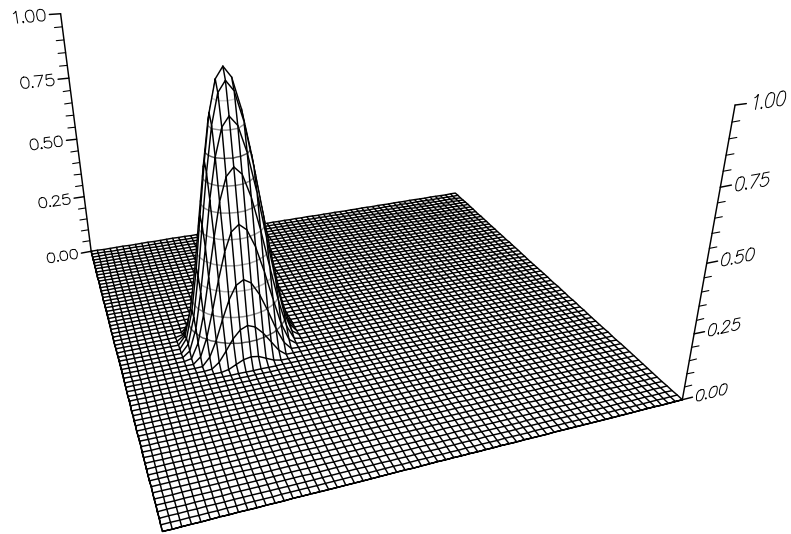
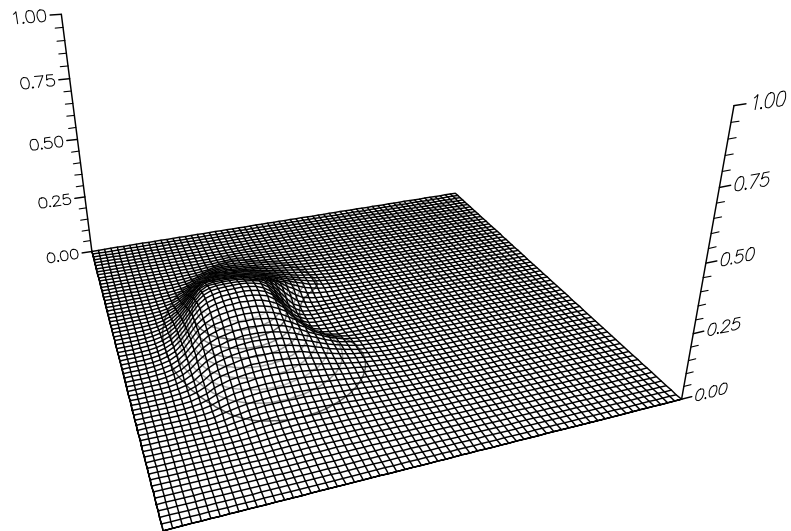Figure 2.21: Rotating cone test case: initial conditions.

Figure 2.22: Rotating cone test case with $t = 1$, one rotation: $\vec{a} = (-2\pi y, 2\pi x)$, VKI NN scheme, grid B.

3 Extension to the Euler Equations

The schemes presented in the previous section have all been developed to solve the linear advection equation in two dimensions, but they can also be considered as an integral part of the solution of systems of nonlinear conservation laws such as the Euler equations,

$$\frac{\partial \underline{u}}{\partial t} + \frac{\partial \underline{F}}{\partial x} + \frac{\partial \underline{G}}{\partial y} = \underline{0}, \tag{3.1}$$

where

$$\underline{u} = \begin{pmatrix} \rho \\ \rho u \\ \rho v \\ e \end{pmatrix}, \quad \underline{F} = \begin{pmatrix} \rho u \\ \rho u^2 + p \\ \rho uv \\ u(p+e) \end{pmatrix}, \quad \underline{G} = \begin{pmatrix} \rho v \\ \rho uv \\ \rho v^2 + p \\ v(p+e) \end{pmatrix}, \tag{3.2}$$

in which ρ is density, u and v are the x- and y-velocities, p is pressure, and e is total energy, related to the other variables by an equation of state which, for a perfect gas, is

$$e = \frac{p}{\gamma - 1} + \frac{1}{2}\rho(u^2 + v^2). \tag{3.3}$$

3.1 A Conservative Linearisation

The Euler equations in the form (3.1) cannot immediately be solved using the multidimensional upwinding techniques described in this paper. Instead, it is necessary to consider the quasilinear form

$$\frac{\partial \underline{u}}{\partial t} + A\frac{\partial \underline{u}}{\partial x} + B\frac{\partial \underline{u}}{\partial y} = \underline{0}, \tag{3.4}$$

where $A = \frac{\partial \underline{F}}{\partial \underline{u}}$ and $B = \frac{\partial \underline{G}}{\partial \underline{u}}$ are the local Jacobian matrices of the system. It is this system which must be discretised over the domain and then solved. In order to achieve this, consistent approximations to the Jacobians A and B are required within each cell, which can be calculated using the nodal values of the data.

In one dimension a conservative approximation to the Jacobian is obtained by requiring the approximate Jacobian to satisfy a property U [22]. In two dimensions the linearisation is forced to be conservative by constructing the local approximations to the Jacobians, $\tilde{A}$ and $\tilde{B}$, so that they satisfy the following two-dimensional version of property U:

- The linearisation is consistent, in the sense that

$$\tilde{A}(\underline{u}, \underline{u}, \underline{u}) = A(\underline{u}), \quad \tilde{B}(\underline{u}, \underline{u}, \underline{u}) = B(\underline{u}). \tag{3.5}$$

- For all angles θ, the matrix $(\tilde{A}(\underline{u}_1, \underline{u}_2, \underline{u}_3)\cos\theta + \tilde{B}(\underline{u}_1, \underline{u}_2, \underline{u}_3)\sin\theta)$ has real eigenvalues and a complete set of linearly independent eigenvectors.

- The identities

$$\widehat{\frac{\partial \mathbf{F}}{\partial x}} \equiv \tilde{A}(\underline{\mathbf{u}}_1, \underline{\mathbf{u}}_2, \underline{\mathbf{u}}_3)\, \widehat{\frac{\partial \underline{\mathbf{u}}}{\partial x}}, \qquad \widehat{\frac{\partial \mathbf{G}}{\partial y}} \equiv \tilde{B}(\underline{\mathbf{u}}_1, \underline{\mathbf{u}}_2, \underline{\mathbf{u}}_3)\, \widehat{\frac{\partial \underline{\mathbf{u}}}{\partial y}}, \qquad (3.6)$$

are satisfied for any $\underline{\mathbf{u}}_1$, $\underline{\mathbf{u}}_2$, $\underline{\mathbf{u}}_3$.

The third of these criteria is critical since it ensures that the linearisation is conservative and is crucial for sharply capturing steady discontinuities. However, it requires that consistent averages, $\widehat{\frac{\partial \mathbf{F}}{\partial x}}$, $\widehat{\frac{\partial \mathbf{G}}{\partial y}}$, $\widehat{\frac{\partial \underline{\mathbf{u}}}{\partial x}}$ and $\widehat{\frac{\partial \underline{\mathbf{u}}}{\partial y}}$, be found for the gradients within each cell.

It could now be assumed that $\underline{\mathbf{u}}$, the vector of conserved variables, varies linearly over each triangular cell, so $\vec{\nabla}\underline{\mathbf{u}}$ is constant within each cell. This unfortunately leads to extremely complicated expressions for the matrix approximations, $\tilde{A}$ and $\tilde{B}$ [30] so, as in one dimension, a set of 'parameter vector' variables is defined,

$$\underline{\mathbf{w}} = \rho^{\frac{1}{2}}(1, u, v, H)^T, \qquad (3.7)$$

where H is the enthalpy, and it is these that are assumed to be linear within each cell. The variables $\underline{\mathbf{u}}$, $\mathbf{F}$ and $\mathbf{G}$ can now be simply expressed as quadratic functions of the components of $\underline{\mathbf{w}}$. Now, since $\vec{\nabla}\underline{\mathbf{w}}$ is constant within each cell,

$$\iint \left(\frac{\partial \mathbf{F}}{\partial x} + \frac{\partial \mathbf{G}}{\partial y} \right) dx\, dy = \iint \left(A_w(\underline{\mathbf{w}}) \frac{\partial \underline{\mathbf{w}}}{\partial x} + B_w(\underline{\mathbf{w}}) \frac{\partial \underline{\mathbf{w}}}{\partial y} \right) dx\, dy$$
$$= \left(\iint A_w(\underline{\mathbf{w}})\, dx\, dy \right) \frac{\partial \underline{\mathbf{w}}}{\partial x} + \left(\iint B_w(\underline{\mathbf{w}})\, dx\, dy \right) \frac{\partial \underline{\mathbf{w}}}{\partial y}, \qquad (3.8)$$

which gives local approximations to the Jacobians in the parameter vector variables, $A_w = \frac{\partial \mathbf{F}}{\partial \underline{\mathbf{w}}}$ and $B_w = \frac{\partial \mathbf{G}}{\partial \underline{\mathbf{w}}}$, which can be expressed as

$$\tilde{A}_w(\underline{\mathbf{w}}_1, \underline{\mathbf{w}}_2, \underline{\mathbf{w}}_3) = \frac{1}{S_T} \iint A_w(\underline{\mathbf{w}})\, dx\, dy$$
$$\tilde{B}_w(\underline{\mathbf{w}}_1, \underline{\mathbf{w}}_2, \underline{\mathbf{w}}_3) = \frac{1}{S_T} \iint B_w(\underline{\mathbf{w}})\, dx\, dy. \qquad (3.9)$$

Now, since the components of A_w and B_w vary linearly over each cell, the integrals reduce to taking arithmetic means, and result in

$$\tilde{A}_w(\underline{\mathbf{w}}_1, \underline{\mathbf{w}}_2, \underline{\mathbf{w}}_3) = A_w(\overline{\underline{\mathbf{w}}}), \qquad \tilde{B}_w(\underline{\mathbf{w}}_1, \underline{\mathbf{w}}_2, \underline{\mathbf{w}}_3) = B_w(\overline{\underline{\mathbf{w}}}) \qquad (3.10)$$

where $\overline{\underline{\mathbf{w}}}$ is simply the arithmetic mean of the values of $\underline{\mathbf{w}}$ at the vertices of the cell. This provides the means to evaluate consistent approximations to the cell fluctuations (or residuals) quickly and simply using

$$\widehat{\frac{\partial \mathbf{F}}{\partial x}} = A_w(\overline{\underline{\mathbf{w}}}) \frac{\partial \underline{\mathbf{w}}}{\partial x}, \qquad \widehat{\frac{\partial \mathbf{G}}{\partial y}} = B_w(\overline{\underline{\mathbf{w}}}) \frac{\partial \underline{\mathbf{w}}}{\partial y}. \qquad (3.11)$$

Note that the cell gradients are calculated using

$$\vec{\nabla}\underline{\mathbf{w}} = \frac{1}{2S_T} \sum_{i=1}^{3} \underline{\mathbf{w}}_i \, \vec{n}_i, \tag{3.12}$$

where S_T is the area of the triangle, $\underline{\mathbf{w}}_i$ is the value of the parameter vector at vertex i of the cell, and $\vec{n}_i$ is the inward normal to the edge opposite vertex i, scaled with the length of that edge.

It is now possible to find the fluctuation in terms of these approximations to the conserved variables by considering the matrix $M_w = \frac{\partial \underline{\mathbf{u}}}{\partial \underline{\mathbf{w}}}$. Immediately, this gives

$$\widehat{\frac{\partial \mathbf{u}}{\partial x}} = M_w(\overline{\underline{\mathbf{w}}})\frac{\partial \mathbf{w}}{\partial x}, \qquad \widehat{\frac{\partial \mathbf{u}}{\partial x}} = M_w(\overline{\underline{\mathbf{w}}})\frac{\partial \mathbf{w}}{\partial x}, \tag{3.13}$$

which can be used in (3.11) to give

$$\widehat{\frac{\partial \mathbf{F}}{\partial x}} = A_w(\overline{\underline{\mathbf{w}}})M_w^{-1}(\overline{\underline{\mathbf{w}}})\frac{\partial \mathbf{u}}{\partial x}, \qquad \widehat{\frac{\partial \mathbf{G}}{\partial y}} = B_w(\overline{\underline{\mathbf{w}}})M_w^{-1}(\overline{\underline{\mathbf{w}}})\frac{\partial \mathbf{u}}{\partial y}, \tag{3.14}$$

and leads finally, by identification with (3.6), to the approximations

$$\tilde{A}(\underline{\mathbf{u}}_1, \underline{\mathbf{u}}_2, \underline{\mathbf{u}}_3) = A(\overline{\underline{\mathbf{w}}}), \qquad \tilde{B}(\underline{\mathbf{u}}_1, \underline{\mathbf{u}}_2, \underline{\mathbf{u}}_3) = B(\overline{\underline{\mathbf{w}}}), \tag{3.15}$$

which were sought to satisfy property U. It is easily checked that the first two parts of property U are also satisfied by these approximations.

It should be noted here that much of the work which follows uses the Euler equations in terms of the primitive variables

$$\underline{\mathbf{q}} = (\rho, u, v, p)^T \tag{3.16}$$

for simplicity. The equations in quasilinear form then become

$$\frac{\partial \underline{\mathbf{q}}}{\partial t} + A'\frac{\partial \underline{\mathbf{q}}}{\partial x} + B'\frac{\partial \underline{\mathbf{q}}}{\partial y} = \underline{\mathbf{0}} \tag{3.17}$$

where

$$A' = M_q^{-1}AM_q, \qquad B' = M_q^{-1}BM_q, \qquad M_q = \frac{\partial \underline{\mathbf{u}}}{\partial \underline{\mathbf{q}}}, \tag{3.18}$$

with A and B as in (3.4). However the conservative linearisation is retained by describing the residual/fluctuation in terms of the conserved variables

$$\underline{\mathbf{R}}_T = -\frac{\phi_T}{S_T} = \tilde{M}_q \left(\tilde{A}'\frac{\partial \underline{\mathbf{q}}}{\partial x} + \tilde{B}'\frac{\partial \underline{\mathbf{q}}}{\partial y} \right), \tag{3.19}$$

where

$$\frac{\partial \underline{\mathbf{q}}}{\partial x} = \tilde{M}_q^{-1}\tilde{M}_w\frac{\partial \underline{\mathbf{w}}}{\partial x}, \qquad \frac{\partial \underline{\mathbf{q}}}{\partial y} = \tilde{M}_q^{-1}\tilde{M}_w\frac{\partial \underline{\mathbf{w}}}{\partial y}. \tag{3.20}$$

It should be noted that consistent matrix approximations, $\tilde{M}_q$, $\tilde{M}_w$, $\tilde{A}'$, $\tilde{B}'$, etc. may be obtained by evaluating them as functions of the cell average parameter vector variables $\overline{\underline{\mathbf{w}}}$ [32], as can any of the cell averaged quantities, such as the conserved variables and the primitive variables.

3.2 Simple Waves

The problem which now arises is due to the fact that the Jacobian matrices A and B which arise from the Euler equations in two dimensions do not share a common set of eigenvectors, and so the linearised system cannot be decoupled immediately into a set of simple advection equations. To overcome this, Roe [25] suggested expressing the fluctuation as a sum of simple wave solutions.

Consider the conservative linearisation of the Euler equations in the primitive variables.

$$\frac{\partial \underline{\mathbf{q}}}{\partial t} + \tilde{A}' \widehat{\frac{\partial \underline{\mathbf{q}}}{\partial x}} + \tilde{B}' \widehat{\frac{\partial \underline{\mathbf{q}}}{\partial y}} = \underline{\mathbf{0}} \tag{3.21}$$

A simple wave solution of this system takes the form

$$\underline{\mathbf{q}} = \underline{\mathbf{q}}(\zeta), \qquad \zeta = \vec{x} \cdot \vec{n}_\theta - \lambda_\theta t, \tag{3.22}$$

where $\vec{n}_\theta = (\cos\theta, \sin\theta)$ gives the direction of propagation and λ_θ the speed of the wave. In fact

$$\vec{\nabla}\underline{\mathbf{q}} = \frac{d\underline{\mathbf{u}}}{d\zeta}\vec{n}_\theta, \tag{3.23}$$

and substituting these into (3.21) gives

$$-\lambda_\theta \frac{d\underline{\mathbf{u}}}{d\zeta} + (\tilde{A}'\cos\theta + \tilde{B}'\sin\theta)\frac{d\underline{\mathbf{u}}}{d\zeta} = \underline{\mathbf{0}}. \tag{3.24}$$

Therefore, $\frac{d\underline{\mathbf{u}}}{d\zeta}$ is a right eigenvector of the matrix $\tilde{A}'\cos\theta + \tilde{B}'\sin\theta$ and λ_θ is the corresponding eigenvalue. Now for each direction θ there exist four distinct eigenvectors with corresponding eigenvalues, each of which corresponds to a different type of wave. In the primitive variables these correspond to an entropy wave,

$$\lambda = u\cos\theta + v\sin\theta, \qquad \underline{\mathbf{r}} = (1, 0, 0, 0)^T, \tag{3.25}$$

a shear wave,

$$\lambda = u\cos\theta + v\sin\theta, \qquad \underline{\mathbf{r}} = \rho\,(0, \sin\theta, -\cos\theta, 0)^T, \tag{3.26}$$

and two acoustic waves,

$$\lambda = u\cos\theta + v\sin\theta \pm c, \qquad \underline{\mathbf{r}} = \frac{1}{2}\left(\frac{\rho}{c}, \pm\cos\theta, \pm\sin\theta, \rho c\right)^T. \tag{3.27}$$

A more complete description of the derivation and effect of these simple waves can be found in [8, 3].

The eigenvectors of the Euler equations in conserved variables can easily be obtained using the transformation

$$\underline{\mathbf{r}}_{cons} = \tilde{M}_q\underline{\mathbf{r}}_{prim}, \tag{3.28}$$

where $\tilde{M}_q$ is the approximation to M_q, (3.18). The eigenvalues remain unchanged.

Now, the assumption that the parameter vector variables vary linearly in space implies that their gradients are constant at a particular time level within each cell. Thus, consistent cell averaged values of the gradients of the primitive variables can be found using (3.20) and these can be expressed within each cell as the superposition of a number of discrete waves

$$\vec{\nabla}\,\underline{\mathbf{q}} = \sum_k \alpha^k\,\underline{\bar{\mathbf{r}}}^k\,\vec{n}^k, \tag{3.29}$$

where $\underline{\bar{\mathbf{r}}}^k$ is a cell averaged value of the eigenvector which has the corresponding eigenvalue $\bar{\lambda}^k$. This corresponds to a sum of waves of strength α_k propagating in the direction of the unit vector $\vec{n}_k$ with speed $\bar{\lambda}^k$.

Now from (3.19), the cell residual can be expressed as

$$\underline{\mathbf{R}}_T = -\frac{\phi_T}{S_T} = \tilde{M}_q \sum_k \alpha^k\,\bar{\lambda}^k\,\underline{\bar{\mathbf{r}}}^k = \sum_k \alpha^k\,\bar{\lambda}^k\,\underline{\bar{\mathbf{r}}}^k_{cons}, \tag{3.30}$$

where $\underline{\bar{\mathbf{r}}}^k_{cons}$ are the eigenvectors corresponding to the conserved variables. Note that this implies that it is only the eigenvectors which are altered by a change of variables and that the wave speeds $\bar{\lambda}^k$ and wave strengths α^k are independent of such changes.

It is also important to note that the velocities $\bar{\lambda}^k\vec{n}^k$ which are obtained for this system are the frontal velocities, or the gradient dependent advection velocities of the previous section. The simple advection velocities required by the linear schemes have to be found in some other manner.

Although an arbitrary flow gradient can be decomposed into a sum of simple wave contributions as in (3.29), if the decomposition is to be matched with a locally linear variation of the flow, $\vec{\nabla}\underline{\mathbf{q}}$ is constant within each cell and there are only 8 degrees of freedom available, corresponding to the x- and y-derivatives of each of the four components of $\underline{\mathbf{q}}$. In one dimension this simple wave analysis leads to a unique decomposition into one entropy wave and two acoustic waves [8] but in two dimensions the decomposition is no longer unique since it involves an arbitrary parameter which corresponds to the wave propagation direction, $0 \le \theta < 2\pi$. Therefore, there are infinitely many possible simple wave solutions to the linearised system, so a strategy is required for the decomposition of the flow into a finite number of linear waves using the conservative linearisation described above and having the desired number of degrees of freedom. These waves can then be treated individually and the residual (fluctuation) distributed according to one of the schemes from the previous section.

3.3 Roe's Wave Models

Roe [23, 25] was one of the first to propose a suitable wave decomposition, using simple wave theory as the basis for his model. He suggested that a finite number of 'active' waves should be selected to represent the flow and reduce the decomposition (3.29) to a limited number of terms. Although there are many such wave models that have the 8 free parameters to fit the 8 degrees of freedom, there are four that appear in the literature, chosen for their simplicity (they give simple real-valued expressions for all data) and their realistic representation of the flow.

Each of these models has four orthogonal waves representing acoustic disturbances, *ie.* acoustic waves at angles θ, $\theta + \frac{\pi}{2}$, $\theta + \pi$ and $\theta + \frac{3\pi}{2}$, which provides five free parameters, the angle θ (taken to be in the range $[-\frac{\pi}{4}, +\frac{\pi}{4}]$ as one of the four waves is bound to lie there) and four strengths α_1, α_2, α_3 and α_4. All the models also have an entropy wave which uses an angle ϕ and a strength β as two more free parameters.

Where the four models differ is in the choice of the final parameter which is defined by

A A uniform vorticity with unknown strength ω. This has the problem that the vorticity does not have a direction associated with it and so it is not clear how the fluctuation due to it should be distributed. A slight variant of this model has recently been proposed by Rudgyard [19] which represents the vorticity as two orthogonal shear waves, thus removing the problem with distributing the vorticity term.

B A shear wave with unknown strength k travelling perpendicular to the streamlines. This model has been found to give particularly good results for isolated shear waves but is inadequate in its modelling of shocks and is only valid for steady flow. Whereas the three other models have 6 'active' waves, this one only has 5, since a shear wave travelling perpendicular to the streamlines has zero gradient dependent advection speed (zero eigenvalue) and so does not contribute to the fluctuation.

C A shear wave with unknown strength k travelling in the direction of the pressure gradient. This produces better results for shock waves but the pressure gradient vanishes near isolated shears so the model is not well defined here.

D A shear wave with unknown strength k travelling at 45° to the acoustic waves. This has been deduced from a kinematic analysis of the Euler equations [29] and appears to overcome all of the problems associated with the first three wave models. It uses the fact that an isolated shock is aligned

with the principal axes of the strain rate tensor while an isolated shear wave is oriented at 45° to these axes. It is this model that is considered by Roe to be the most promising, so it is the one which will be concentrated on from now on.
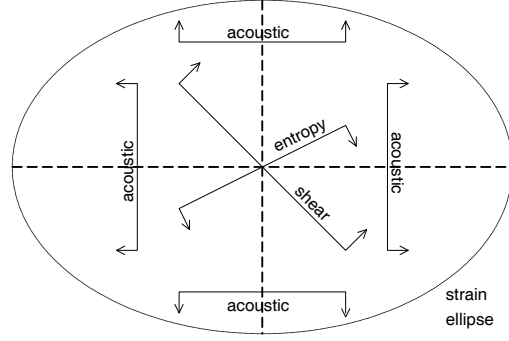

Figure 3.1: Graphical representation of Roe's wave model D.

Another model of similar type is due to Parpia [14] and consists of two parallel acoustic waves, two orthogonal shear waves and an entropy wave, giving five wave strengths and three angles as the eight unknowns.

Once the simple waves have been chosen they must then be substituted into the decomposition of the flow gradient (3.29). With model D this leads to the following set of 8 equations in the 8 unknowns, the wave strengths α_1, α_2, α_3, α_4, β and k, and the directions θ and ϕ.

$$\frac{1}{\rho}\frac{\partial \rho}{\partial x} = \alpha_1 \cos\theta + \alpha_2 \cos\theta - \alpha_3 \sin\theta - \alpha_4 \sin\theta + \beta \cos\phi$$

$$\frac{1}{\rho}\frac{\partial \rho}{\partial y} = \alpha_1 \sin\theta + \alpha_2 \sin\theta - \alpha_3 \cos\theta - \alpha_4 \cos\theta + \beta \sin\phi$$

$$\frac{1}{c}\frac{\partial u}{\partial x} = \alpha_1 \cos^2\theta - \alpha_2 \cos^2\theta + \alpha_3 \sin^2\theta - \alpha_4 \sin^2\theta - k \sin\zeta \cos\zeta$$

$$\frac{1}{c}\frac{\partial u}{\partial y} = \alpha_1 \sin\theta\cos\theta - \alpha_2 \sin\theta\cos\theta - \alpha_3 \sin\theta\cos\theta + \alpha_4 \sin\theta\cos\theta - k \sin^2\zeta$$

$$\frac{1}{c}\frac{\partial v}{\partial x} = \alpha_1 \sin\theta\cos\theta - \alpha_2 \sin\theta\cos\theta - \alpha_3 \sin\theta\cos\theta + \alpha_4 \sin\theta\cos\theta + k \cos^2\zeta$$

$$\frac{1}{c}\frac{\partial v}{\partial y} = \alpha_1 \sin^2\theta - \alpha_2 \sin^2\theta + \alpha_3 \cos^2\theta - \alpha_4 \cos^2\theta + k \sin\zeta \cos\zeta$$

$$\frac{1}{\rho c^2}\frac{\partial p}{\partial x} = \alpha_1 \cos\theta + \alpha_2 \cos\theta - \alpha_3 \sin\theta - \alpha_4 \sin\theta$$

$$\frac{1}{\rho c^2}\frac{\partial p}{\partial y} = \alpha_1 \sin\theta + \alpha_2 \sin\theta + \alpha_3 \cos\theta + \alpha_4 \cos\theta, \tag{3.31}$$

where ζ the angle of the shear wave is defined by

$$\zeta = \theta - \frac{\pi}{4} sign\left(\frac{\partial v}{\partial x} - \frac{\partial u}{\partial y}\right). \tag{3.32}$$

33

The other three wave models differ only in the choice of the sixth wave, so the only alterations to the above equations required are in the terms involving the strength k and the direction ζ.

This system can be easily solved for the unknown strengths and angles [23] to get them in terms of the gradients of the primitive variables. The resulting acoustic waves propagate in directions parallel to the principal strain rate axes of the local flow, as desired in the kinematic analysis, and the shear wave strength turns out to be the local vorticity within the cell. Solving for the direction and strength of the entropy wave gives precisely the direction and modulus of the entropy gradient.

Each of the waves now has a strength α^k, an eigenvalue (speed) $\overline{\lambda}^k$, an eigenvector $\underline{\mathbf{r}}^k$ and a direction θ_k which can be substituted into (3.30) to produce the fluctuations due to each simple wave. These can then be distributed using one of the schemes described in the previous section.

3.4 Rudgyard's Wave Models

More recently Rudgyard [18, 19] has proposed an alternative wave decomposition which again uses simple waves but is derived by a slightly different approach. This can be considered as a mesh independent directional splitting technique which uses the fact (shown earlier) that for a particular direction θ there are four types of wave, corresponding to an entropy wave, a shear wave and two acoustic waves. It also makes use of the identity

$$\vec{\nabla}\,\underline{\mathbf{q}} \equiv \frac{-(\vec{s}_{\theta_2} \cdot \vec{\nabla}\,\underline{\mathbf{q}})\vec{n}_{\theta_1} + (\vec{s}_{\theta_1} \cdot \vec{\nabla}\,\underline{\mathbf{q}})\vec{n}_{\theta_2}}{\sin(\theta_2 - \theta_1)}, \tag{3.33}$$

where $\vec{s}_\theta = (-\sin\theta, \cos\theta)$ is the unit vector orthogonal to $\vec{n}_\theta$. The wave model is obtained by projecting each term on the right hand side of (3.33) on to the eigenvectors corresponding to the angles θ_1 and θ_2 respectively, to give

$$\vec{\nabla}\,\underline{\mathbf{q}} = \sum_{k=1}^{4} \alpha_{\theta_1}^{(k)}\,\underline{\mathbf{r}}_{\theta_1}^{(k)}\,\vec{n}_{\theta_1} + \sum_{k=1}^{4} \alpha_{\theta_2}^{(k)}\,\underline{\mathbf{r}}_{\theta_2}^{(k)}\,\vec{n}_{\theta_2}, \tag{3.34}$$

where

$$\alpha_{\theta_1}^{(k)} = -\frac{\vec{s}_{\theta_2} \cdot (\underline{\mathbf{l}}_{\theta_1}^{(k)}\,\vec{\nabla}\,\underline{\mathbf{q}})}{\sin(\theta_2 - \theta_1)}, \qquad \alpha_{\theta_2}^{(k)} = \frac{\vec{s}_{\theta_1} \cdot (\underline{\mathbf{l}}_{\theta_2}^{(k)}\,\vec{\nabla}\,\underline{\mathbf{q}})}{\sin(\theta_2 - \theta_1)}. \tag{3.35}$$

These are the 8 wave strengths which are the free parameters for this model. The $\underline{\mathbf{l}}_{\theta_i}^{(k)}$ are the left eigenvectors of the matrix $\tilde{A}'\cos\theta + \tilde{B}'\sin\theta$ with corresponding right eigenvectors $\underline{\mathbf{r}}_{\theta_i}^{(k)}$.

A number of different wave models can be derived by choosing the definition of the angles θ_1 and θ_2. An obvious choice is $\theta_1 = 0$ and $\theta_2 = \frac{\pi}{2}$ for which the discrete x- and y-derivatives are treated independently. However, it is far more

beneficial to select the angles with a view to minimising the number of 'active' waves present in the decomposition by choosing directions which set either the strength or speed of particular waves to zero. This means that these waves do not contribute to the decomposition of the fluctuation and so reduces the computational effort. Alternatively, the angles can be chosen to align with physically important gradients to improve the shock capturing capabilities of the method [33].

Now, the eigenvectors for the entropy waves are independent of the direction, so the number of waves present in the model can be reduced by combining them to form one wave. It turns out that the single entropy wave produced has a strength and direction which are simply the modulus and direction of the entropy gradient, as was the case with each of Roe's models. The gradient decomposition can now be written

$$
\vec{\nabla}\,\underline{\mathbf{q}} = \sum_{k=1}^{3} \alpha_{\theta_1}^{(k)}\,\underline{\mathbf{r}}_{\theta_1}^{(k)}\,\vec{n}_{\theta_1} + \sum_{k=1}^{3} \alpha_{\theta_2}^{(k)}\,\underline{\mathbf{r}}_{\theta_2}^{(k)}\,\vec{n}_{\theta_2} + \alpha_\phi\,\underline{\mathbf{r}}_\phi\,\vec{n}_\phi, \tag{3.36}
$$

A five wave model can be obtained by choosing

$$
\theta_1 = \tan^{-1}\left(\frac{\frac{\partial p}{\partial y}}{\frac{\partial p}{\partial x}}\right), \qquad \theta_2 = \tan^{-1}\left(\frac{\frac{\partial u}{\partial x}\frac{\partial p}{\partial y} - \frac{\partial u}{\partial y}\frac{\partial p}{\partial x}}{-\frac{\partial v}{\partial x}\frac{\partial p}{\partial y} + \frac{\partial v}{\partial y}\frac{\partial p}{\partial x}}\right), \tag{3.37}
$$

which sets the strengths of two of the acoustic waves, $\alpha_{\theta_2}^{(1)}$ and $\alpha_{\theta_2}^{(2)}$, to zero. The resulting decomposition has an entropy wave, two acoustic waves and a shear wave based on the angle θ_1, and a single shear wave based on θ_2.

Alternatively, the angles can be chosen to set wave speeds to zero so that although the waves appear in the gradient decomposition, they make no contribution to the fluctuation. A 'streamwise' splitting involves setting $\underline{\mathbf{n}}_{\theta_1}$ and $\underline{\mathbf{n}}_{\theta_2}$ to be parallel and orthogonal to the streamlines, which makes the speed of one of the shear waves zero. The 'Mach angle' splitting sets the speed of two sound waves to zero by choosing

$$
\theta_1 = \tan^{-1}\left(\frac{v + u(M^2 - 1)^{\frac{1}{2}}}{u - v(M^2 - 1)^{\frac{1}{2}}}\right), \qquad \theta_2 = \tan^{-1}\left(\frac{v - u(M^2 - 1)^{\frac{1}{2}}}{u + v(M^2 - 1)^{\frac{1}{2}}}\right), \tag{3.38}
$$

where $M = (u^2 + v^2)^{\frac{1}{2}}/c$ is the Mach number. The remaining acoustic waves then propagate at angles which correspond to the characteristics of the steady supersonic Euler equations, the Mach angles. Unfortunately these angles are not defined for subsonic flow, so the scheme has to be modified, replacing the terms $(M^2 - 1)$ by $\max(\epsilon, |M^2 - 1|)$, introducing the parameter ϵ to avoid the singularity in the wave strengths when $\sin(\theta_2 - \theta_1) = 0$. This is clearly unsatisfactory for problems with large regions of subsonic flow.

Finally, a four wave model may also be obtained by these methods. It is based on a five wave model involving two parallel acoustic waves, two shear waves and

an entropy wave. One of the shear waves is then chosen to be orthogonal to the streamlines, forcing its speed to be zero. Four wave models have a great appeal in the context of accuracy. When more waves are used, the fluctuation, a four-vector, is decomposed into more than four discrete waves and so a zero residual does not generally give zero wave strengths. In fact, a locally steady flow is represented as a state of equilibrium between the discrete waves [23] and, in the above models, only the entropy wave is guaranteed to have zero strength. This is contrary to the philosophy of the fluctuation distribution schemes of section 2, and of cell vertex methods in general, for which a zero fluctuation within a cell should imply a null contribution to its nodes. In particular it calls into question the usefulness of requiring a scalar distribution scheme to satisfy linearity preservation in order to improve its accuracy, when this could be largely negated by the wave model used. Rudgyard [19] describes in more detail how decompositions may be derived to overcome these problems and suggests that four wave models may represent the way forward.

3.5   The Deconinck/Hirsch Wave Model

A third separate approach to wave decomposition has been proposed by Deconinck, Hirsch and Peuteman [10]. Unlike the previous methods it does not consider simple waves, but is based on converting the Euler equations to a set of maximally decoupled scalar advection equations by using characteristic theory. No results from this wave model are presented in this report but some may be found in [32] where it is studied in conjunction with a number of the distribution schemes presented in section 2.

The quasilinear system (3.4) can be transformed to a set of characteristic variables $\underline{\mathbf{W}}$ using the matrix $M_W = \frac{\partial \underline{\mathbf{u}}}{\partial \underline{\mathbf{W}}}$, giving

$$\frac{\partial \mathbf{W}}{\partial t} + M_W^{-1} A M_W \frac{\partial \mathbf{W}}{\partial x} + M_W^{-1} B M_W \frac{\partial \mathbf{W}}{\partial y} = \underline{\mathbf{0}}. \tag{3.39}$$

It is not possible to decouple the system by choosing M_W such that $M_W^{-1} A M_W$ and $M_W^{-1} B M_W$ are both diagonal since A and B do not commute. Instead M_W and $\underline{\mathbf{W}}$ are sought which satisfy

$$M_W^{-1} A M_W = D^x + C^x, \qquad M_W^{-1} B M_W = D^y + C^y, \tag{3.40}$$

with

$$C^x \frac{\partial \mathbf{W}}{\partial x} + C^y \frac{\partial \mathbf{W}}{\partial y} = \underline{\mathbf{0}}, \tag{3.41}$$

where D^x and D^y are diagonal matrices. The Euler equations would then become

$$\frac{\partial \mathbf{W}}{\partial t} + D^x \frac{\partial \mathbf{W}}{\partial x} + D^y \frac{\partial \mathbf{W}}{\partial y} = \underline{\mathbf{0}}, \tag{3.42}$$

a set of four decoupled equations.

In [8] it is shown how the Euler equations can be written as an equivalent set of compatibility relations. These can be written as

$$\frac{\partial W^1}{\partial t} + \vec{u}\,\vec{\nabla}W^1 = 0 \quad with \quad \partial W^1 = \partial\rho - \frac{1}{c^2}\partial p$$

$$\frac{\partial W^2}{\partial t} + \vec{u}\,\vec{\nabla}W^2 + \frac{1}{\rho}\vec{s}^{\,2}\cdot\vec{\nabla}p = 0 \quad with \quad \partial W^2 = \vec{s}^{\,2}\cdot\partial\vec{u}$$

$$\frac{\partial W^3}{\partial t} + (\vec{u}+c\,\vec{n}^3)\vec{\nabla}W^3 + c\,\vec{s}^{\,3}\cdot(\vec{s}^{\,3}\cdot\vec{\nabla})\vec{u} = 0 \quad with \quad \partial W^3 = \vec{n}^3\cdot\partial\vec{u} + \frac{1}{\rho c}\partial p$$

$$\frac{\partial W^4}{\partial t} + (\vec{u}-c\,\vec{n}^4)\vec{\nabla}W^4 + c\,\vec{s}^{\,4}\cdot(\vec{s}^{\,4}\cdot\vec{\nabla})\vec{u} = 0 \quad with \quad \partial W^4 = -\vec{n}^4\cdot\partial\vec{u} + \frac{1}{\rho c}\partial p$$

$$(3.43)$$

where the $\vec{s}^{\,i}$ are unit vectors normal to $\vec{n}^i$, the direction of propagation of the wavefront in the x-y plane, and $\vec{u} = (u,v)^T$ is the velocity vector.

This set of compatibility relations can now be identified with the decoupled system (3.42) provided that the coupling terms in the last three equations can be made to vanish. This can be done by choosing a particular characteristic surface such that locally

$$\vec{s}^{\,2}\cdot\vec{\nabla}p = 0, \qquad \vec{s}^{\,3}\cdot(\vec{s}^{\,3}\cdot\vec{\nabla})\vec{u} = 0, \qquad \vec{s}^{\,4} = \vec{s}^{\,3}. \qquad (3.44)$$

The first condition is easily satisfied and corresponds to a shear wave propagating in the direction of the local pressure gradient. The conditions on $\vec{s}^{\,3}$ and $\vec{s}^{\,4}$ are more complicated. The coupling term in the third and fourth equations can be written in terms of the local strain rate tensor, ε, giving

$$c\,\vec{s}\cdot(\vec{s}\cdot\vec{\nabla})\vec{u} = c\,(\vec{s}^{\,T}\varepsilon\vec{s}) = \vec{0}, \qquad (3.45)$$

where

$$\varepsilon = \begin{pmatrix} \frac{\partial u}{\partial x} & \frac{1}{2}\left(\frac{\partial u}{\partial y}+\frac{\partial v}{\partial x}\right) \\ \frac{1}{2}\left(\frac{\partial v}{\partial x}+\frac{\partial u}{\partial y}\right) & \frac{\partial v}{\partial y} \end{pmatrix}, \qquad (3.46)$$

Now (3.45) has two real solutions for $\vec{s}$ only if ε has eigenvalues, λ_X, λ_Y, of different sign, and so a complete decoupling can be obtained by choosing $\vec{s}$ to b one of these solutions.

Otherwise, the coupling term cannot be set to zero, so it is instead minimised by choosing $\vec{s}$ to be along the principal axis corresponding to the minimum strain rate in the fluid giving

$$c\,\vec{s}\cdot(\vec{s}\cdot\vec{\nabla})\vec{u} = c\,\min(|\lambda_X|,|\lambda_Y|). \qquad (3.47)$$

An optimally decoupled system has now been obtained which is of the form

$$\frac{\partial\mathbf{W}}{\partial t} + D^x\frac{\partial\mathbf{W}}{\partial x} + D^y\frac{\partial\mathbf{W}}{\partial y} + \underline{\mathbf{Q}}_W = \underline{\mathbf{0}}, \qquad (3.48)$$

where $\underline{\mathbf{Q}}_W$ is the coupling term. If this is zero, which it is for locally subsonic flow and for some regions of supersonic flow, the four equations can be treated separately using one of the fluctuation distribution schemes. The system is therefore considered to consist of an entropy wave, a shear wave and two acoustic waves together with a minimal coupling term which can be treated separately. In practice it is projected on to the four eigenvectors and each component distributed as part of one of the four waves.

3.6 Implementation

We now have a variety of wave models which decompose the Euler equations into a number of simple waves, each of which can then be treated separately. The fluctuation due to each wave within each cell can then be distributed to its vertices using one of the scalar advection schemes described in section 2. All that remains is to define the link between the two.

In practice, this involves deciding on an advection velocity vector, used to calculate the k_i, and a discrete gradient, from which the edge differences can be found using

$$u_i - u_j = (\vec{x}_i - \vec{x}_j) \cdot \vec{\nabla} u, \tag{3.49}$$

where $\vec{x}_i$ is the position vector of node i, and from which the gradient dependent advection velocity can be calculated. These are the only quantities required by any of the schemes of section 2 to distribute the fluctuation due to each wave.

For the Deconinck/Hirsch wave model the discrete gradients correspond to the expressions for the ∂W^i in (3.43) and the simple advection velocities are taken to be the velocity vector for shear and entropy waves, and the bicharacteristic vector for the acoustic waves, so

$$\vec{\lambda}^{e,s} = \vec{u}, \qquad \vec{\lambda}^a = \vec{u} \pm c\vec{n}_\theta^a, \tag{3.50}$$

where $\vec{n}_\theta^a = (\cos\theta, \sin\theta)^T$ is the unit vector in the wave propagation direction θ, and $\vec{u} = (u, v)^T$ is the velocity vector.

However, Rudgyard [19] suggests that the situation when considering a simple wave decomposition of the form (3.30) is not as clear. Most authors define the advection velocities as in (3.50), and there is an implicit assumption in (3.22) that the simple wave front will move in the direction $\vec{n}_\theta$, giving the gradient dependent advection velocities,

$$\vec{\lambda}_m^{e,s} = (\vec{u} \cdot \vec{n}_\theta^{e,s})\vec{n}_\theta^{e,s}, \qquad \vec{\lambda}_m^a = (\vec{u} \cdot \vec{n}_\theta^a \pm c)\vec{n}_\theta^a. \tag{3.51}$$

This only ensures the correct treatment of the entropy wave and that the advection vectors lie within the domain of dependence of the unsteady problem.

However, it is these values which are used to produce all the results in the next section which are obtained using Roe's wave models.

As an example, Rudgyard refers to his own Mach angle splitting and notes that a component corresponding to a projection on to an eigenvector $\underline{\mathbf{r}}_{\theta_1}$ will only be advected in the direction $\vec{n}_{\theta_1}$ if this is orthogonal to $\vec{n}_{\theta_2}$, and similarly for waves based on $\underline{\mathbf{r}}_{\theta_2}$. His conclusion is that the assumption that all decompositions of the type (3.30) lead to simple waves as defined by (3.22) and (3.24) is false.

He then suggests a better alternative for the Mach angle splitting (3.36) which treats the entropy wave as before, since it is independent of the direction, but changes the shear and acoustic waves. The wave strengths (3.35) lead to

$$
\lambda_{\theta_1}^{(k)} \alpha_{\theta_1}^{(k)} = - \frac{\lambda_{\theta_1} \, \vec{s}_{\theta_2} \cdot (\underline{\mathbf{l}}_{\theta_1}^{(k)} \vec{\nabla} \, \mathbf{q})}{\sin(\theta_2 - \theta_1)}, \qquad \lambda_{\theta_2}^{(k)} \alpha_{\theta_2}^{(k)} = \frac{\lambda_{\theta_2} \, \vec{s}_{\theta_1} \cdot (\underline{\mathbf{l}}_{\theta_2}^{(k)} \vec{\nabla} \, \mathbf{q})}{\sin(\theta_2 - \theta_1)}, \qquad (3.52)
$$

which give the new discrete gradients, $(\underline{\mathbf{l}}_{\theta_i}^{(k)} \vec{\nabla} \, \mathbf{q})$, advection directions, $-\vec{s}_{\theta_2}$ and $\vec{s}_{\theta_1}$, and advection speeds, $\lambda_{\theta_i} / \sin(\theta_2 - \theta_1)$, where the λ_{θ_i} are the moduli of the vectors in (3.51) – the eigenvalues.

He also describes alternatives for Roe's wave models, but only this one is used in the results presented in the next section.

3.7 Results

Results from three test cases introduced by Ni [31] are presented here, all of which are circular arc bump in channel flows. The channel height, and bump length are both unity, and the flow is from left to right across a section of length 3 with the bump at its centre. Each case is run to steady state and can be defined by the freestream Mach number of the flow and the height of the bump as a percentage of the channel height. The three test cases are

1) $M_\infty = 0.5$, 10% bump. This gives a wholly subsonic flow.

2) $M_\infty = 0.675$, 10% bump. This gives a transonic flow with a supersonic region terminated by a shock which should be located at about 72% chord on the bump.

3) $M_\infty = 1.4$, 4% bump. This gives a mainly supersonic flow with two strong, oblique shocks formed at the ends of the bump, the first of which is reflected by the top and then the bottom wall of the channel.

For all these results the grids are produced by subdividing a regular 65×33 cartesian mesh into triangles by inserting diagonals to form one of the three types of grids shown in figure 2.7. Figure 3.2 shows, as an example, the type B grid for the 10% bump test cases. In each case the flow was given initial

conditions of uniform flow at the freestream Mach number and then run until a steady state solution was reached. The flow tangency condition is applied at solid walls while freestream boundaries are treated using a combination extrapolation from the interior and Riemann invariant boundary conditions, depending on the speed and direction of the flow. In all cases local time stepping has been used with a CFL number of 0.8.

The first set of results uses a grid of type B and show Roe's wave model D used with the VKI NN scheme. Figure 3.3 shows a plot of Mach number contours for test case 1) and the same test case using the Lax-Wendroff scheme is shown in figure 3.4. Of the two, Lax-Wendroff is much the better since it does at least give contours which are symmetric about the centre of the bump. The upwind solution seems to 'lean in the wind', particularly near the lower wall, and the problem occurs whichever mesh is used. It may be associated with the solid wall boundary conditions, but is also exhibited by other wave models such as those of Rudgyard and Parpia [14], although the phenomenon is less noticeable in results presented by Roe [21] on a finer mesh.

Figure 3.5 shows the results from using Roe's model D on the second, transonic, test case. Again the plot is of Mach number contours and it shows a shock of about the right strength in the correct position on the bump. It is captured across one cell of the grid, although this isn't generally the case when the shock is not aligned with the grid. This test case has also been considered by Rudgyard [19], but of his methods only the four wave model produces a shock with the correct strength and position, and this unfortunately gives an expansion shock upstream of the desired one, a problem also exhibited by Parpia's five wave model.

Figure 3.6 shows Mach number contours for the third test case using Roe's model D again. Each of the two oblique shocks formed at the ends of the bump are captured well, as are the reflected shocks at both the upper and lower surfaces of the channel. In fact the solution looks very good and, unlike in the scalar case, the shock does not spread out downstream, although the nonlinearity of the system does cause very small oscillations in the solution in front of the first shock which are visible here because of the contour at $M = 1.5$.

The main problem with this model, and with all of the wave models which use the discrete solution gradients directly to calculate the wave propagation directions, is robustness. None of the results presented here which use Roe's scheme have been converged to machine accuracy. The size of the residuals tends to decrease by a couple of orders of magnitude and then start oscillating. Converged solutions to some problems have been achieved and presented [32, 14] but success seems to be dependent on many things such as the problem itself and boundary conditions, so before these schemes become truly useful some method must be devised to increase their robustness. It has been suggested that the source of this

problem is the calculation of the wave directions, and that since they depend on the local flow gradients, which are piecewise constant, they are unable to settle down to a steady state value. Recent work has also been carried out on the non-linear advection schemes to improve their convergence properties when applied to a two-dimensional version of the inviscid Burgers' equation [17] and this may well improve results for the Euler equations as well.

With Rudgyard's models this is not such a serious problem. Some of his wave models, such as his Mach angle splitting, do not use the gradients to calculate the angles, and all solutions presented here which use this model have been converged to machine accuracy. For his other models it is easy to freeze the directions within each cell to attain converged solutions. This, though, is clearly an undesirable method of achieving robustness when time varying flows are considered. Also, it is not obvious how to freeze or lag these angles for Roe's models since their calculation involves solving a set of 8 equations (3.31).

This gives Rudgyard's models a significant advantage over those of Roe and others. However, figure 3.8 shows that, for the third test case, his Mach angle splitting identifies each of the shocks which are supposed to be present, but does not give as sharp a definition as Roe's model D. Rudgyard's own results [19] indicate that this difference is not as great as is shown here but he does emphasise that this model is only valid for mainly supersonic flows. He also shows that these multidimensional methods compare favourably with a standard MUSCLE TVD scheme. Both of these wave models though show a huge improvement over Rudgyard's dimensional splitting, figure 3.7, in which none of the shocks are adequately captured.

Figures 3.9 and 3.10, produced with Rudgyard's Mach angle splitting on grids of type A and C, show that the grid dependence seen in the linear advection schemes of the previous section is inherited by these methods, although since the fluctuation is now split into a number of separate waves, all with different directions, the problem is not as noticeable. It is still obvious though that discontinuities are captured much more sharply if they are aligned with the diagonals of the grid, *eg.* the shock formed at the front of the bump is captured more sharply by the type A grid, indicating that it may again be possible to use grid adaption to great effect. Roe's wave model is more susceptible to the vagaries of grid generation and the problem of robustness becomes even more apparent when an unfavourable grid is used. However, it also means that on a grid where the cell edges are aligned with the shocks Roe's wave model gives much sharper discontinuities than Rudgyard's model. This grid dependence should be solely due to the orientation of the flow relative to the mesh edges, and therefore only depend on the propagation directions of the simple waves, since the wave model itself is independent of the grid.
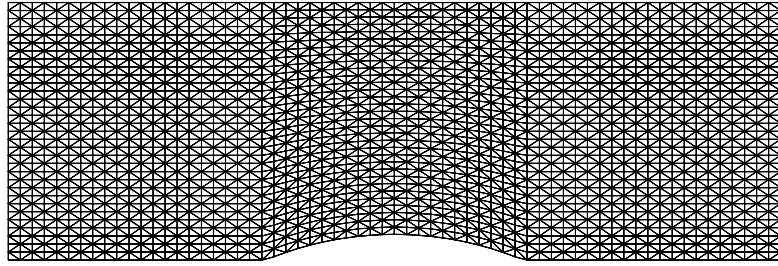
Figure 3.2: Representative grid (type B) for the 10% circular arc bump in channel test cases.
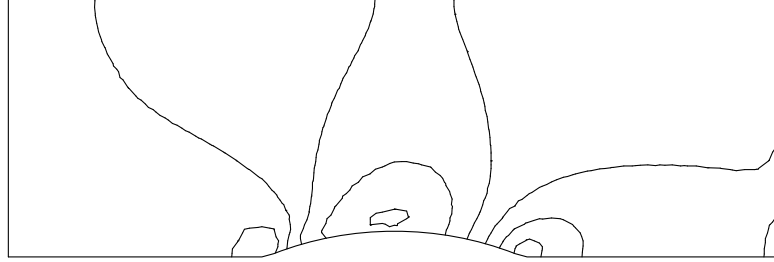
Figure 3.3: $M_\infty = 0.5$, 10% bump using Roe's model D and the VKI NN scheme on grid B. Mach number contours with interval 0.05.
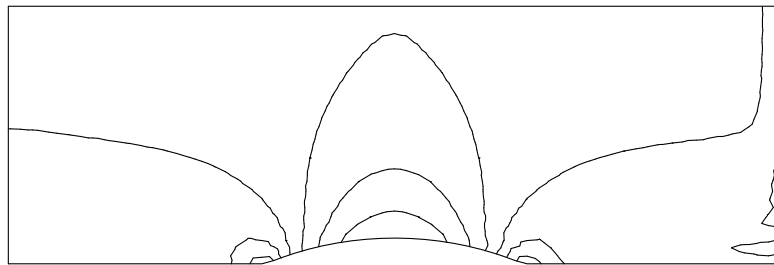

Figure 3.4: $M_\infty = 0.5$, 10% bump using the Lax-Wendroff scheme on grid B. Mach number contours with interval 0.05.
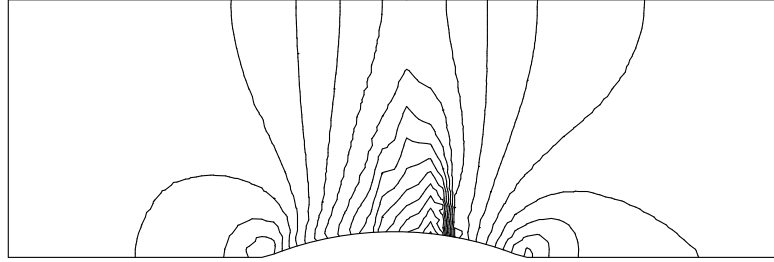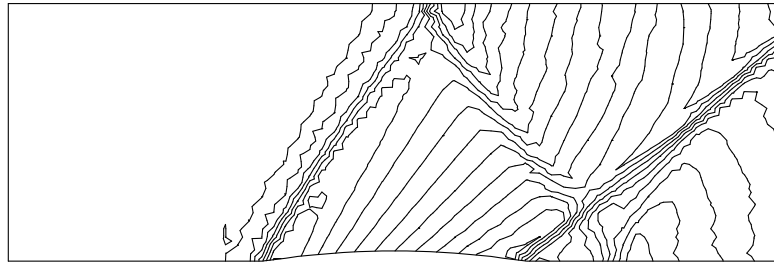
Figure 3.5: $M_\infty = 0.675$, 10% bump using Roe's model D and the VKI NN scheme on grid B. Mach number contours with interval 0.05.

Figure 3.6: $M_\infty = 1.4$, 4% bump using Roe's model D and the VKI NN scheme on grid B. Mach number contours with interval 0.05.
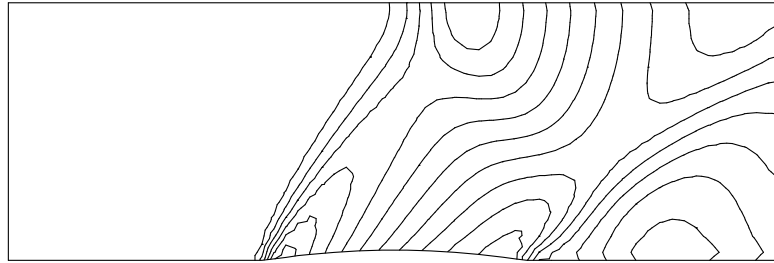
Figure 3.7: $M_\infty = 1.4$, 4% bump using Rudgyard's dimensional splitting and the VKI NN scheme on grid B. Mach number contours with interval 0.05.
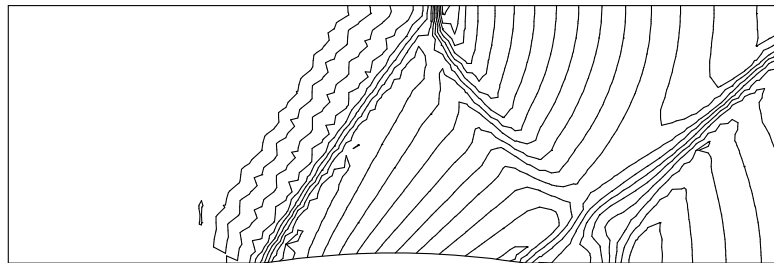

Figure 3.8: $M_\infty = 1.4$, 4% bump using Rudgyard's Mach angle splitting and the VKI NN scheme on grid B. Mach number contours with interval 0.05.
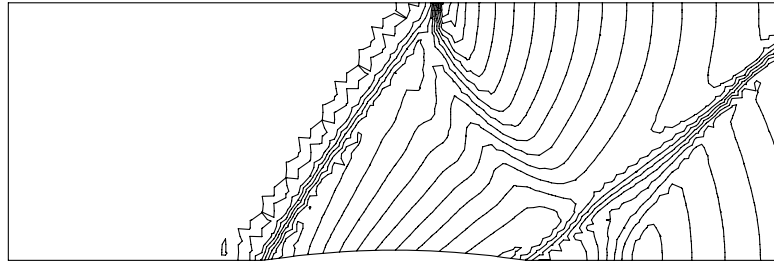
Figure 3.9: $M_\infty = 1.4$, 4% bump using Rudgyard's Mach angle splitting and the VKI NN scheme on grid A. Mach number contours with interval 0.05.
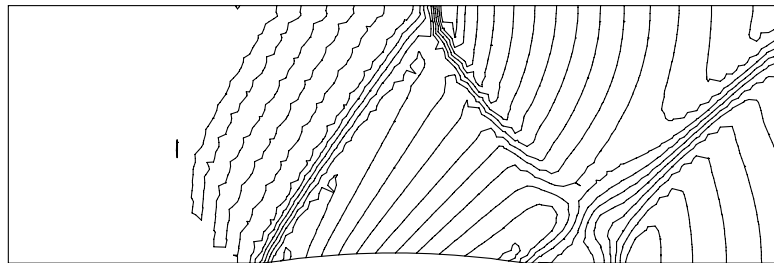

Figure 3.10: $M_\infty = 1.4$, 4% bump using Rudgyard's Mach angle splitting and the VKI NN scheme on grid C. Mach number contours with interval 0.05.

4   A Hybrid Approach

Many points have been highlighted by a large number of authors in the study of the methods described in this report. Probably the most important is that multidimensional upwinding schemes are still very much in the early stages of their development. However, even now there are indications as to the strengths and weaknesses of these methods.

At present it seems that, although these methods are good at modelling discontinuous flow features such as shocks and shears, they are inadequate for the smoother, purely subsonic flows. However, subsonic flow and smooth flow in general can be modelled very well by far less complicated schemes, such as the Lax-Wendroff type scheme described in section 2.3. This suggests that this scheme could be used throughout the smooth regions of the flow, while the more expensive multidimensional upwinding techniques are used only in the vicinity of flow features which the simple scheme is unable to cope with, thus considerably reducing the computational effort required. A brief study of the use of such a hybrid approach in one dimension has been conducted with considerable success [20].

Just one set of results is presented here, since this work has only just begun. In this case a monitor has been introduced to detect shocks which simply consists of checking the density gradient within each cell. During each time step all the cells with a density gradient over a specified value were flagged, as were all adjacent cells. Then, in every flagged cell, multidimensional upwinding was used (in this case Rudgyard's Mach angle splitting with the VKI NN-scheme), while the Lax-Wendroff scheme was used everywhere else. To increase the robustness of the method it was necessary to ensure that cells did not alternate between schemes every few time steps. This was achieved by first introducing a lag so that a cell, once flagged, retained the flag for at least the next 100 iterations and secondly, as the steady state was approached, a flagged cell became permanently flagged. The pictures shown are of results which have been converged to machine precision.

Figure 4.1 shows the Mach number contours, plotted at intervals of 0.05, for the hybrid scheme used on a 65×33 grid of type B, where multidimensional upwinding is used in cells where $\vec{\nabla}\rho > 2$ and in adjacent triangles (these cells are superimposed in figure 4.2). Even at this early stage the results are encouraging. The solution is very close to that using upwinding alone, figure 3.8, although, if anything, the shocks are captured more sharply. The one obvious problem is the wiggles that can be seen downstream of the interface 'corners', such as those coming off the top of the isolated group of upwinded cells near the centre of the domain, figure 4.2, and parallel to the stronger shocks. This type of phenomenon is not unexpected and is similar to that seen in one dimension [20] when hybrid

methods were used. There, it was resolved by moving the interface between the regions where the two schemes were used further away from the shock. While this may well remove the wiggles parallel to the shocks, it will probably have little effect on the 'corner' wiggles which are intrinsically multidimensional phenomena.

One of the big advantages of using the hybrid scheme is its speed. A single Lax-Wendroff time step takes roughly one third the cpu time of a single time step using multidimensional upwinding (although this varies depending on the scheme used). In this hybrid calculation there were never more than 20% of the cells using upwinding (in fact it settled down to 702 out of 4096) for a flow in which relatively large regions are close to shocks. This converged hybrid solution was produced in less than 40% of the time it took to calculate the completely upwinded result, a figure which would be reduced for flows with weaker and fewer shocks.
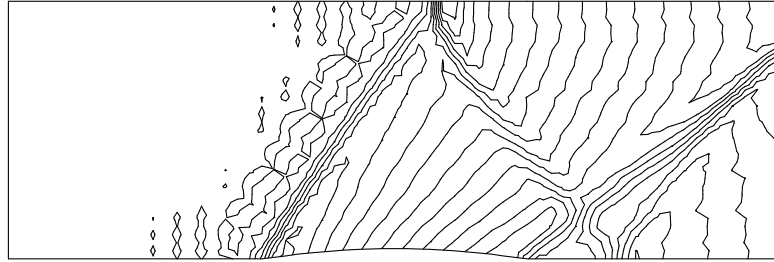
Figure 4.1: $M_\infty = 1.4$, 4% bump using Rudgyard's Mach angle splitting and the VKI NN scheme for $\vec{\nabla}\rho > 2$ and Lax-Wendroff elsewhere on grid B.
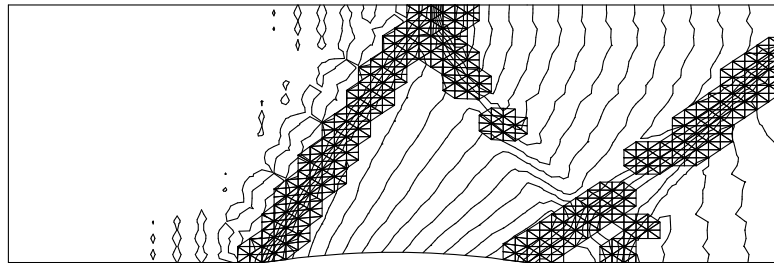

Figure 4.2: $M_\infty = 1.4$, 4% bump using Rudgyard's Mach angle splitting and the VKI NN scheme for $\vec{\nabla}\rho > 2$ and Lax-Wendroff elsewhere on grid B, with the cells using the upwind scheme superimposed.

5 Conclusions

It is obvious from the results presented in this report and by other authors that these genuinely multidimensional methods are still in the early stages of their development. However, compact schemes have been developed for use on triangular and tetrahedral meshes which show much promise for the future.

Of the two main aspects of the work, the fluctuation distribution schemes are probably the better understood. Optimal linear positive and linearity preserving schemes have been developed, although it is necessary to consider nonlinear schemes before one can be both positive (monotone) and linearity preserving (second order). The so-called nonlinear narrow schemes are generally considered to be the best of those presented, although it is not clear which of the variants is the most promising.

Common to all of these schemes is a grid dependence. Discontinuities are captured far more sharply if they are roughly aligned with the edges of the grid cells. While this at first seems undesirable, it could easily be turned to advantage by developing new adaption techniques which align cell edges with discontinuities. Also, while these schemes adequately model steady state problems, more work is needed before they can be used with any confidence to produce time varying solutions.

The wave decomposition models pose completely different questions. These are independent of the grid, but solutions to the two-dimensional Euler equations for flow in a bumpy channel still show a dependence on the grid, inherited from the advection schemes, although this is greatly reduced from the scalar case.

As yet it is unclear which wave model will prove to be the best, or even whether specific decompositions might be better for different flow features. Results using two models, Roe's model D and Rudgyard's Mach angle splitting, are shown in this report. Roe's wave model seems to give good resolution of shocks but suffers from problems with convergence. Rudgyard's is the more robust but only gives good results for mainly supersonic flows. For flows with large subsonic regions, his four wave model is better although it has a tendency to produce expansion shocks. The convergence problems of Roe's scheme seem to be shared by all of the wave models where the wave propagation directions depend on the discrete flow gradients and it is not clear how this can be overcome. Also none of the methods can model wholly subsonic, shock-free flows as well as a simple Lax-Wendroff type scheme.

One option for future research is the development of hybrid methods which use schemes locally which are appropriate to the type of flow being modelled. This means that a cheap scheme can be used for smooth regions of flow, where upwinding is less reliable, while the more expensive, genuinely multidimensional

scheme is only used close to more 'interesting' parts of the flow. Initial results indicate that results can be obtained by this method which are of similar quality to those produced using multidimensional methods alone, but in less than 40% of the time.

Acknowledgements

References

[1] A.Dadone and B.Grossman. A rotated upwind scheme for the Euler equations. Paper 91-0635, AIAA, 1991.

[2] A.Jameson and D.Mavriplis. Finite volume solution of the two-dimensional Euler equations on a regular triangular mesh. *AIAA Journal*, 24:611–618, 1986.

[3] A.Majda. *Compressible Fluid Flow and Systems of Conservation Laws in Several Space Variables*, volume 53 of *Applied Mathematical Sciences*. Springer-Verlag, 1984.

[4] C.L.Rumsey, B.van Leer, and P.L.Roe. A grid-independent approximate Riemann solver with applications to the Euler and Navier-Stokes equations. Paper 91-1530, AIAA, 1991.

[5] D.W.Levy. *Use of a Rotated Riemann Solver for the Two-Dimensional Euler Equations*. PhD thesis, University of Michigan, 1990.

[6] D.W.Levy, K.G.Powell, and B.van Leer. Implementation of a grid-independent upwind scheme for the Euler equations. In *AIAA 9th Computational Fluid Dynamics Conference*, 1989.

[7] G.T.Tomaich and P.L.Roe. Compact schemes for advection-diffusion problems on unstructured grids. *Modelling and Simulation*, 23(5):2629, 1993.

[8] H.Deconinck. Upwind methods and multidimensional splittings for the Euler equations. In *VKI Lecture Series 1991-01 'Computational Fluid Dynamics'*, 1991.

[9] H.Deconinck. Beyond the Riemann problem II. In *Algorithmic Trends in Computational Fluid Dynamics for the 90's*, 1992. ICASE - NASA Langley Workshop, September 1991.

[10] H.Deconinck, C.Hirsch, and J.Peuteman. Characteristic decomposition methods for the multidimensional Euler equations. In *Lecture Notes in Physics 264 '10th Int. Conf. on Numerical Methods in Fluid Dynamics'*, pages 216–221. Springer Verlag, 1986.

[11] H.Deconinck, R.Struijs, G.Bourgois, H.Paillere, and P.L.Roe. Multidimensional upwind methods for unstructured grids. In *Unstructured Grid Methods for Advection Dominated Flows*, May 1992. AGARD Report 787.

[12] H.Deconinck, R.Struijs, and P.L.Roe. Fluctuation splitting for multidimensional convection problems: an alternative to finite volume and finite element methods. In *VKI Lecture Series 1990-03 'Computational Fluid Dynamics'*, March 1990.

[13] I.H.Parpia. A planar oblique wave model for the Euler equations. Paper 91-1545, AIAA, 1991.

[14] I.H.Parpia and D.J.Michalek. Grid-independent upwind scheme for multidimensional flow. *AIAA Journal*, 31(4):646–651, April 1993.

[15] J.-D.Muller and P.L.Roe. Experiments on the accuracy of some advection schemes on unstructured and partly structured grids. *Modelling and Simulation*, 23(5):2645, 1993.

[16] B.van Leer. Progress in multi-dimensional upwind differencing. Report 92-43, ICASE, 1992.

[17] L.M.Mesaros and P.L.Roe. Analysis of multidimensional upwinding schemes on triangular grids, 1992.

[18] M.A.Rudgyard. A comparison of multidimensional upwinding for cell vertex schemes on triangular meshes. In *Numerical Methods for Fluid Dynamics V*, 1992. In publication.

[19] M.A.Rudgyard. Multidimensional wave decompositions for the Euler equations. In *VKI Lecture Series 1993-04 'Computational Fluid Dynamics'*, 1993. VKI Lecture Notes.

[20] M.E.Hubbard. A hybrid central/upwind approach to the solution of the one dimensional Euler equations. Report 2/93, Department of Mathematics, University of Reading, 1993.

[21] P.L.Roe. Multidimensional upwinding. Lecture Notes.

[22] P.L.Roe. Approximate Riemann solvers, parameter vectors, and difference schemes. *J. Comp. Phys.*, 43(2):357–372, October 1981.

[23] P.L.Roe. A basis for upwind differencing of the two-dimensional unsteady Euler equations. In K.W.Morton and M.J.Baines, editors, *Numerical Methods for Fluid Dynamics II*, pages 55–80. Oxford University Press, 1986.

[24] P.L.Roe. Characteristic-based schemes for the Euler equations. *Ann. Rev. Fluid Mech.*, 18:337–365, 1986.

[25] P.L.Roe. Discrete models for the numerical analysis of time-dependent multidimensional gas dynamics. *J. Comp. Phys.*, 63:458–476, 1986.

[26] P.L.Roe. Optimum upwind advection on triangular meshes. Technical Report 90-75, ICASE, 1990.

[27] P.L.Roe. Beyond the Riemann problem I. In *Algorithmic Trends in Computational Fluid Dynamics for the 90's*, 1992. ICASE - NASA Langley Workshop, September 1991.

[28] P.L.Roe and D.Sidilkover. Optimum positive linear schemes for advection in two and three dimensions. *SIAM J. Numer. Anal.*, 29(6):1542–1568, December 1992.

[29] P.L.Roe and L.Beard. An improved wave model for multidimensional upwinding of the Euler equations. In M.Napolitano and F.Sabetta, editors, *Proceedings of the 13th International Conference on Numerical Fluid Dynamics*, Lecture Notes in Physics, Issue 414, page 135, 1993.

[30] P.L.Roe, R.Struijs, and H.Deconinck. A conservative linearisation of the multidimensional Euler equations. *J. Comp. Phys.*, 1993. To appear.

[31] R.H.Ni. A multiple grid scheme for solving the Euler equations. *AIAA Journal*, 20(11):1565–1571, 1982.

[32] R.Struijs, P.L.Roe, and H.Deconinck. Fluctuation splitting schemes for the 2d Euler equations. In *VKI Lecture Series 1991-01 'Computational Fluid Dynamics'*, 1991.

[33] S.F.Davis. A rotationally biased upwind difference scheme for the Euler equations. *J. Comp. Phys.*, 56:65–92, 1984.

[34] S.P.Speckreijse. Multigrid solution of monotone second order discretisations of hyperbolic conservation laws. *Math. Comp.*, 49:135–155, 1987.

[35] Y.Tamara and K.Fujii. A multidimensional upwind scheme for the Euler equations on unstructured grids. In M.M.Hafez, editor, *4th ISCFD Conference*, 1991.

Appendix - A Brief Note on Notation

Due to the complexity of the subject and the huge variety of notation that has been used by a large number of different authors, it seems necessary to include a brief explanation of some of the notation in this report. I have tried to strike a balance between continuing the conventions of previous authors and making this report self-consistent. Unfortunately, few previous papers have presented work on both distribution schemes and wave models and this is reflected here in that there are some inconsistencies in the notation between sections 2 and 3.

The following points should be noted when reading this report.

- The sets of flow variables which are used are

    - $\underline{\mathbf{u}}$ – conserved variables.

    - $\underline{\mathbf{w}}$ – parameter vector variables.

    - $\underline{\mathbf{W}}$ – characteristic variables.

    - $\underline{\mathbf{q}}$ – primitive variables.

    In particular, $\underline{\mathbf{u}}$ should not be confused in section 3 with u, the x-velocity, or $\vec{u}$, the cartesian velocity vector. This is in line with Roe's notation, although he also tends to use $\underline{\mathbf{u}}$ as the primitive variables.

- Four-vectors such as the flow variables are shown in bold font and underlined, *eg.* $\underline{\mathbf{u}}$, while two-vectors in the space variables x and y are written with arrows over the top, $\vec{a}$. This convention, or something similar, has been adopted by most authors.

- S_T is always a grid cell area while S_i is always a median dual grid cell area. More generally, a subscript or superscript T indicates a quantity associated with a cell, while a subscript i or j indicates a nodal quantity.

All other notation should be clear from the description given in the text or the context in which it is presented.